國 立 交 通 大 學

電 子 物 理 研 究 所

碩 士 論 文

850 nm 離子佈植型面射型雷射之製造與光輸出－電流曲線之斜率特性分析

Fabrication of 850 nm Implanted VCSELs with Characterization of Slope Efficiencies in L-I Curves

研 究 生：王世賢

指導教授：楊賜麟 博士

中 華 民 國 九 十 三 年 十 月

850 nm 離子佈植型面射型雷射之製造與光輸出－電流曲線之斜率特性分析

Fabrication of 850 nm Implanted VCSELs with Characterization of Slope Efficiencies in L-I Curves

研 究 生：王世賢　　Student：S. H. Wang

指導教授：楊賜麟　博士　　Advisor：Dr. S. L. Yang

國 立 交 通 大 學

電 子 物 理 研 究 所

碩 士 論 文

A Thesis

Submitted to Institute of Electrophysics

College of Science

National Chiao Tung University

in Partial Fulfillment of the Requirements

for the Degree of

Master

in

ElectroPhysics

September 2004

Hsinchu, Taiwan, Republic of China

中華民國九十三年十月

850 nm 離子佈植型面射型雷射之製造與光輸出—電流曲線之斜率特性分析

研究生：王世賢　　　　　　　　　　　　　　　指導教授：楊賜麟 博士

國立交通大學電子物理研究所

摘要

我們在面射型雷射元件離子佈植製程步驟前成長二氧化矽層，使接觸金屬和電極能夠同時蒸鍍，並且在室溫直流條件下做晶片量測。元件之間的差異在於成長不同厚度的二氧化矽層以及在光罩設計下不同的離子佈植及接觸金屬的孔徑尺寸。

在離子佈植前成長較薄的二氧化矽層對離子佈植深度影響較小，同時元件的特性也較佳。不同離子佈植及接觸金屬孔徑的元件，其基本光輸出—電流—電壓特性的量測結果亦符合其相關電流散佈及熱的性質。在離子佈植型雷射一般光譜特性的量測結果中可以顯現出其與橫模波長間的關係。空間增益缺陷及熱透鏡效應對離子佈植型雷射橫模的生成，和光輸出—電流曲線中扭曲的現象和變動的斜率是有關聯的，其量測結果亦符合離子佈植孔徑尺寸的相關問題。最後比較估計的基態橫模寬度和接觸金屬的孔徑尺寸可以得到當面射型雷射元件的接觸金屬開口越小時，不但使輸出在相對較低階橫模的操作電流區間增長，也可得到更線性的光輸出特性。較小孔徑的接觸金屬抑制了高階態橫模的輸出，同時它也減輕了因為高階態橫模的生成，而在光輸出—電流曲線中所造成的扭曲問題。

Fabrication of 850 nm Implanted VCSELs with Characterization of Slope Efficiencies in L-I Curves

Student: S. H. Wang Advisor: Dr. S. L. Yang

Institute of ElectroPhysics
National Chiao Tung University

ABSTRACT

We fabricated the implanted VCSELs with SiO_2 deposited before implantation to evaporate the metal contacts and pads at the same time and the wafer-level testing was performed under continuous-wave operation at room temperature. The devices are different in SiO_2 thickness with various implant and contact aperture sizes through the mask design.

A thinner SiO_2 deposition before ion implantation has less affect to ion projection range and provides a better device performance. The basic L-I-V characteristics of the devices with different implant and contact apertures are performed with the results conforming to the related current spreading and thermal properties. The general behavior of emission spectrum for implanted VCSELs in relation to the wavelengths of transverse modes is also applied. The transverse mode formation in implanted VCSELs corresponding to the spatial hole burning and thermal lens effects is related to the kink phenomenon in L-I curves with variant slope efficiency and the results are reasonable for the implant aperture size problem. Finally, the estimated fundamental mode width compared with the contact aperture sizes implies that reducing the diameter of the contact opening in VCSEL devices not only extends the operating current range for the output with lower order modes but also provides more linear output characteristic. The contact opening with smaller diameter suppresses the output with higher order modes and it alleviates the kink problem in an L-I curve originated from the higher-order mode formation.

誌謝

首先感謝指導教授楊賜麟老師，以及威凱科技公司徐總經理的大力協助，還有工程師劭斌、彥鈞、巧薇、佳美、靜寧、淑樺等在過程中給我的幫忙，特別是劭斌學長在繁忙工作中不吝費時地在製程上給了我許多建議及幫助，在此特別感激。另外要感謝的是核能研究所耿台成先生的協助，其熱心程度讓我印象非常深刻，在此也要特別感謝。最後要感謝我的父母對我的支持與鼓勵，謝謝你們！

Contents

摘要……………………………………………………………………………………i

Abstract………………………………………………………………………………..ii

誌謝……………………………………………………………………………………..iii

Contents………………………………………………………………………………iv

Captions of Figures…………………………………………………………………...vi

Chapter 1 Introduction……………………………………………………..1

Chapter 2 Fundamental Issues of VCSELs………………………….3

2.1 Fundamental Theories…………………………………………………………...3

2.1.2 Rate Equations……………………………………………………………..3

2.1.2 Threshold Condition………………………………………………………5

2.2 Mirrors…………………………………………………………………………….8

2.2.1 Bragg Condition……………………………………………………………9

2.2.2 Design of DBRs…………………………………………………………..10

2.3 Optical Cavities…………………………………………………………………...11

2.3.1 Gain in Active Region……………………………………………………12

2.3.2 Design of Optical Cavities………………………………………………..13

2.4 Various Types of VCSELs……………………………………………………….13

1896

2.4.1 Etched-Pillar VCSELs……………………………………………………14

2.4.2 Etched/Regrown VCSELs…………………………………………………..15

2.4.3 Ion-Implanted VCSELs…………………………………………………..16

2.4.4 Selectively Oxidized VCSELs……………………………………………..16

Chapter 3 Experiment……………………………………………………..**18**

Chapter 4 Result and Discussion……………………………………**23**

4.1 Ion Implantation……………………………………………………………..23

4.2 L-I-V Characteristics…………………………………………………………..26

4.3 Emission Spectrum……………………………………………………………32

4.4 Slope Efficiencies in L-I Curves…………………………………………………34

4.4.1 Gain and Index Guiding……………………………………………………..34

4.4.2 Spatial Hole Burning and Self-Focusing Effects………………..…………35

4.4.3 Kink and Slope Efficiency………………………………………………..36

4.4.4 Fundamental Mode Size and Contact Apertures……………………38

Chapter 5 Conclusion……………………………….………………………**46**

References…………………………………………………………………………**48**

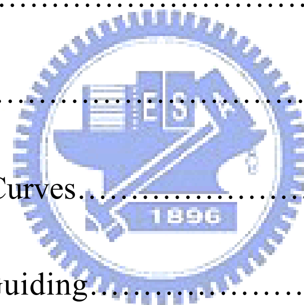

Captions of Figures

Figure 2.1 A brief sketch of the VCSEL structure……………………………………………5
Figure 2.2 The optical property of the DBR structures……………………………………8
Figure 2.3 The (a) heterostructure and (b) optical field distribution in the cavity………..11
Figure 2.4 The structures of (a) etched-pillar, (b) etched/regrown, (c) ion-implanted, (d) selectively oxidized VCSELs……………………………………………………..14

Figure 3.1 The process procedures of the device with (a) original wafer, (b) SiO_2 deposition, (c) ion implantation, and (d) metal evaporation…………………20
Figure 3.2 The top view image of the device……………………………………………..20

Figure 4.1 The implantation depths of the devices with different SiO_2 thickness………..25
Figure 4.2 The output characteristics of the devices with different SiO_2 thickness……...25
Figure 4.3 The I-V characteristics of the devices with different implant aperture sizes…28
Figure 4.4 The I-V characteristics of the devices with different contact aperture sizes….28
Figure 4.5 The series resistance of the devices with different aperture sizes…………….29
Figure 4.6 The L-I characteristics of the devices with different implant aperture sizes….29
Figure 4.7 The L-I characteristics of the devices with different contact aperture sizes….30
Figure 4.8 The threshold current (density) of the devices with different aperture sizes….30
Figure 4.9 (a) The gain/cavity mismatch and (b) the thermal roll-over effect……………31
Figure 4.10 The peak power and current range of the devices with different implant aperture sizes………………………………………………………………31
Figure 4.11 The peak power and current range of the devices with different contact aperture sizes………………………………………………………………………..32
Figure 4.12 The emission spectrum of the implanted VCSEL…………………………….34
Figure 4.13 (a) The gain guiding for the implanted VCSEL and (b) the index guiding for the oxidized VCSEL…………………………………………………………41
Figure 4.14 The spatial hole burning effect starts with (a) the initial gain above threshold and (b) the increasing intensity of light reduces the gain in the middle along with the injection current. Finally the gain in the surroundings eventually above threshold and the higher order mode starts to lase……………..……..41
Figure 4.15 (a) The self-focusing (thermal lens) effect and (b) the kink of the L-I curve corresponding to the transverse mode formation…………………………….42
Figure 4.16 The slope efficiency in relation to the kink in the L-I curve………………….42
Figure 4.17 The power, slope efficiency, and the current range according to the selected bias point in the devices with different implant aperture sizes………………43

Figure 4.18 The power, slope efficiency, and the current range according to the selected bias point in the devices with different contact aperture sizes……………….43
Figure 4.19 The power, current range, and spectrum according to the selected bias point in the 12-12 um device……………………………………………………..44
Figure 4.20 The power, current range, and spectrum according to the selected bias point in the 4-12 um device………………………………………………………44
Figure 4.21 The variation of the slope efficiency of the L-I curve from threshold to roll-over in the 12-12 um device…………………………………………...45
Figure 4.22 The variation of the slope efficiency of the L-I curve from threshold to roll-over in the 4-12 um device……………………………………………45

Chapter 1

Introduction

In the late 1970's, Iga and his coworkers at Tokyo Institute of Technology, published a paper about an InGaAsP/InP laser with a mirror directly formed on the epitaxial surface with the other one on the opposite side of the substrate to form a vertical cavity producing the laser emission normal to the crystal growth surface [1]. This novel design was very creative compared to the original edge-emitting lasers, but didn't attract much attention due to the poor characteristics in terms of high threshold current and low output power. They continued to improve the device performance and eventually the first room-temperature vertical-cavity surface-emitting laser (VCSEL) under continuous-wave operation was achieved in 1988 [2].

Since the late 1980's, the research of VCSELs has emerged throughout the world. From the studies of basic theories to advances in epitaxial growth and fabrication technology, especially the development of distributed Bragg reflector (DBR) that constitutes the longitudinal laser cavity, the area of VCSELs had been taken seriously and was desirable to the commercial market [3]. Continuous innovations in the design of mirrors, gain structures, and fabrication techniques, VCSELs had taken advantages of conventional edge-emitting lasers in threshold current and efficiency [4,5]. The inherent advantages of VCSELs arose possibilities for various applications such as printing, data storage, and optical interconnecting technology. Hence, several companies began to develop VCSELs toward manufacturing area since the mid 1990's. Presently, commercial products of VCSELs are widely seen and readily to use especially in the local area networks.

The reason why VCSELs attracted much attention and encouraged a wide range of research is because of several advantages over edge-emitting lasers. Conventional edge-emitting lasers need to be fabricated the facet mirrors by cleaving or dry etching

techniques and because of the emission from the edge of the laser chip, optical testing cannot be performed until the packaging process is completed. The cross section of the active region, which is transversely thin for carrier confinement and laterally wide for output power, gives results of elliptical field distribution especially large divergence in the transverse dimension that makes challenges for coupling into the circular optical fiber.

A fundamental difference of VCSELs is the perpendicular emission light from the surface and the wafer testing can be performed without further cleaving or packaging process [6]. The symmetrical circular beam and smaller divergence make VCSELs inherently convenient optical sources for optical fibers and the nature of the emission in the axial direction from the wafer surface makes possibility to fabricate high dense two-dimensional arrays for extensive applications [7]. Also the short cavity of the VCSEL compared to the edge-emitting laser inherently produces a single longitudinal mode without complex processing unlike the special structure designated for the edge-emitting laser to have the same property. Although many advantages of VCSELs mentioned above, restriction of VCSELs due to the reduced volume of the gain medium, high quality mirrors produced by epitaxial growth, and the design for electrical and optical confinements with those processing techniques are still the primary concerns to VCSELs.

Chapter 2

Fundamental Issues of VCSELs

The operation of VCSELs originated from the basic theories applied also to the edge-emitting lasers and the topics involved for VCSELs, such as the design of mirrors and optical cavity with particular properties of those structures, are introduced in this chapter. In the end, various types of VCSEL devices and their process techniques are briefly described.

2.1 Fundamental Theories

2.1.1 Rate Equations

First we consider the creation of light by electron transitions between the conduction and valance bands in semiconductors. Four transitions are considered herein: the spontaneous emission, stimulated absorption, stimulated emission (coherent photon emission), and nonradiative transition. Only the spontaneous and stimulated emission contribute to light generation and their related electron-hole recombination process are designed to perform in the region called the "active region" where the photon emission and useful optical gain achieved in the semiconductor lasers. Electrons and holes supplied by the injection current are confined in the active region due to the high barriers surrounded. The active region is usually intrinsic or lightly doped so the electron density N is close to the hole density in the active region. That is, N can be counted as the density of electrons, holes, or electron-hole pairs in the active region.

The generation rates of carriers in the active region are expressed as

$$\frac{dN}{dt} = \eta_i \frac{I}{qV} - \frac{N}{\tau} - R_{nst}, \tag{2.1}$$

where η_i is internal quantum efficiency representing the fraction of carriers from the

terminal node to be confined in the active region, q is the electron charge, τ is the carrier lifetime, and R_{nst} is the net stimulated recombination rate. The term $\frac{N}{\tau}$ is in composition of various recombination rates,

$$\frac{\mathrm{N}}{\tau} = \mathrm{R}_{\mathrm{sp}} + \mathrm{R}_{\mathrm{nr}} + \mathrm{R}_{\mathrm{l}}, \tag{2.2}$$

where, $\mathrm{R}_{\mathrm{sp}} = \mathrm{BN}^2$, $\mathrm{R}_{\mathrm{nr}} = \mathrm{AN}$, and $\mathrm{R}_{\mathrm{l}} = \mathrm{CN}^3$ represent the spontaneous, nonradiative, and leakage recombination rates, respectively. The leakage can be attributed to the thermionic emission or lateral diffusion if there was no lateral confinement and the carriers flow through the active region without recombination.

We considered the photon density N_p and its rate equation including the photon generation and loss terms,

$$\frac{dN_p}{dt} = \Gamma(R_{st} + \beta_{sp} R_{sp}) - \frac{N_p}{\tau_p}. \tag{2.3}$$

β_{sp} is the spontaneous emission factor, τ_p is the photon lifetime, and Γ is the confinement factor. The recombined carries are usually confined in the active region like quantum wells but the generated photons may occupy the surrounded claddings, i.e., the active region has smaller dimensions than the volume in which the generated light is hold. So Γ represents an overlap factor between the active region dimensions and the electric field profiles, and can be expressed as $\Gamma_{xy}\Gamma_z$ to be separated as the transverse and the axial propagation parts.

The photon-stimulated recombination generates more photons through a gain process in the active region and the gain coefficient g is defined as the increased photon density from an incoming value to an existing value as those photons pass through a small length, e.g., $\Delta N_p = N_p g \Delta z = N_p g v_g \Delta t$, where v_g is the group velocity. We can find out that

$R_{nst} = \Delta N_p / \Delta t = g v_g N_p$ and subscribe to (2.1) and (2.3) to get a set of rate equations that describe the basic time evolutions of the carriers and photons as

$$\frac{dN}{dt} = \eta_i \frac{I}{qV} - \frac{N}{\tau} - g v_g N_p \quad \text{and} \tag{2.4}$$

$$\frac{dN_p}{dt} = \Gamma(g v_g N_p + \beta_{sp} R_{sp}) - \frac{N_p}{\tau_p}. \tag{2.5}$$

2.1.2 Threshold Condition

The VCSEL structure involved with light action is presented in Fig. 2.1. In the laser cavity, the gain or loss is not uniform throughout the volume occupied by the optical modes, just like the confinement factor Γ mentioned before. The defined gain g is referred as the material gain $g(x, y, z)$, a function of three-dimensional space. But the net effect of g contributes to the optical mode is referred as the modal gain $< g >$, an overlap factor that is a weighted average of the gain distribution to the entire cavity volume with respect to the electric field profile.

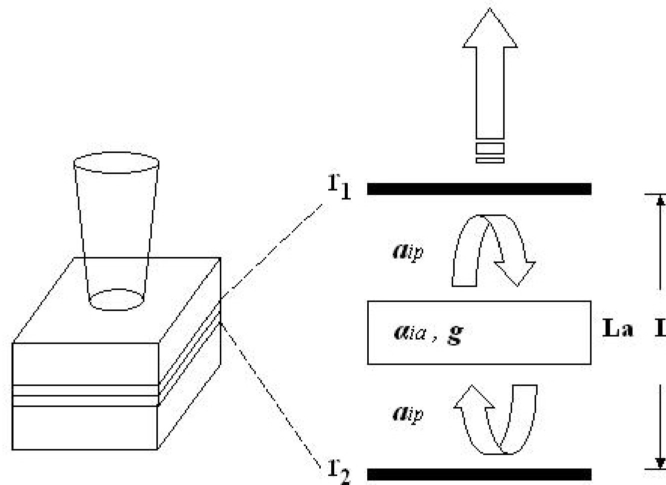

Fig. 2.1 A brief sketch of the VCSEL structure

In order to reach threshold condition for an optical mode, the gain must compensate the

loss resulted from light propagation in the medium and reflection from the mirrors. To the point that the electric filed remains the same amplitude after a round-trip gives the threshold condition and the gain is now referred as the threshold gain $<g>_{th}$. We assume the mode propagates as $e^{j\tilde{\beta}z}$, where

$$\tilde{\beta} = \beta + \frac{j}{2}(<g>_{xy} - <\alpha_i>_{xy}). \quad (2.6)$$

The terms $<g>_{xy}$ and $<\alpha_i>_{xy}$ represent the transverse modal gain and the internal modal loss and will be simplified by $\Gamma_{xy}g$ and α_i if $g(x,y)$ is constant across the active region. The threshold condition occurs when

$$r_1 r_2 e^{-2j\tilde{\beta}_{th}(L_a+L_p)} = 1. \quad (2.7)$$

r is the reflection coefficient and L_a, L_p represent the lengths of the active and passive section of the cavity and the gain in the passive section is zero. From (2.6), (2.7), and the simplified notations we have

$$\Gamma_{xy} g_{th} L_a = \alpha_{ia} L_a + \alpha_{ip} L_p + \ln(\frac{1}{r_1 r_2}).$$

For in-plane case, $\Gamma_{xy} L_a / L \approx \Gamma_{xy}\Gamma_z = \Gamma$ with a defined $<\alpha_i>$ that equals to $(\alpha_{ia} L_a + \alpha_{ip} L_p)/L$ as the average internal loss, we finally get

$$<g>_{th} = \Gamma g_{th} = <\alpha_i> + \frac{1}{L}\ln(\frac{1}{r_1 r_2}). \quad (2.8)$$

This is the general expression of the threshold gain and with a short cavity length L, the reflectance must be increased as well as in VCSELs. As the photon lifetime τ_p explains the photon decay in terms of the propagation and the mirror loss, we can refer the second term of (2.8) as the mirror loss and rewrite it to have the point of view that the gain and the total loss exactly compensate at the threshold condition,

$$\Gamma g_{th} = <\alpha_i> + \alpha_m = \frac{1}{v_g \tau_p}. \tag{2.9}$$

In (2.8), the general form $<g>_{th}$ is valid all the time, but the form Γg_{th} has the limitation $L_a >> \lambda$ for $L_a / L = \Gamma_z$ as we have used above for in-plane lasers. The axial confinement factor Γ_z in very short active region $(L_a << \lambda)$ will be enhanced above the generally-expected value L_a / L by a factor ξ, which corresponds to the locations between the electric filed standing-wave peak and the center of the active region. In the situation of thin active region like VCSELs and the active region is centered on the standing-wave peak in the cavity, the axial confinement factor can be nearly doubled ($\Gamma_z \approx 2L_a / L$). For a multi-quantum-well active region in a VCSEL with N_w wells of thickness L_w, the confinement factor can be expressed as $\Gamma = \Gamma_{xy} \xi N_w L_w / L$.

The gain at threshold has been discussed. The way to reach the value of threshold gain is by increasing the injected carriers/current due to the carrier density in relation to the Fermi-levels. The linear approximation under small-signal condition to the relationship between the gain g and the carrier density N is given by

$$g \approx a(N - N_{tr}), \tag{2.10}$$

where N_{tr} is the transparency carrier density that results in a zero gain and the light will not be amplified and seems to be transparent throughout the region and a is noticed as the differential gain. The relation implies that as we continue to increase the injection current, the increasing gain is expected. But in fact that in steady-state condition above threshold there exits no gain higher than the threshold gain. Because if the gain overcomes the loss and continues to increase, the electric field will go on the same without limits and the steady-state operation in lasers will no longer be formed. According to (2.10) the saturated carrier density N_{th} in steady-state condition above threshold is clearly shown. The additional carriers above N_{th} from the increasing injection current above threshold contribute to the stimulated recombinations and produce the laser output.

2.2 *Mirrors*

Unlike the cleaved facets designed for edge-emitting lasers, mirrors with high reflectivity are demanded in VCSELs due to the short active region length. The use of gratings or distributed Bragg reflectors (DBRs) is widely seen in semiconductor lasers. The wavelength selectivity for single axial mode in in-plane lasers noticed as distributed -feedback (DFB) lasers and the high reflectivity requirement for VCSELs reveals the importance of DBRs to the design of mirrors in laser cavities (Fig.2.2).

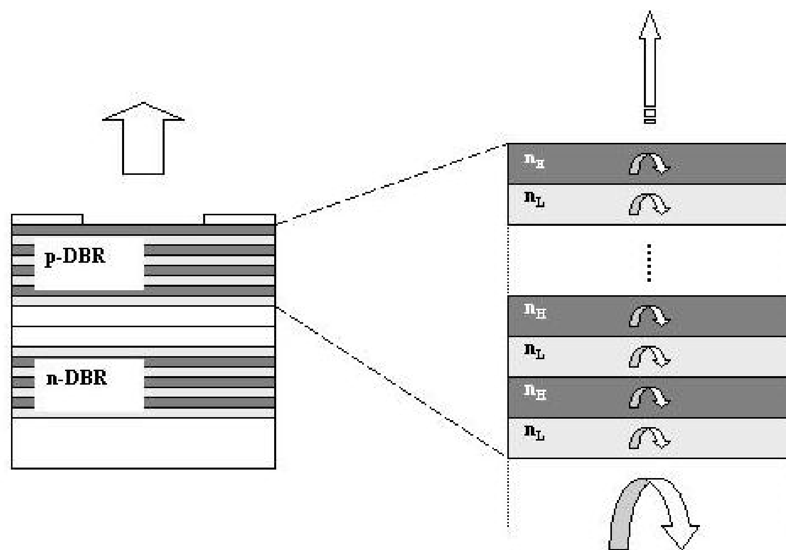

Fig. 2.2 The optical property of the DBR structure

2.2.1 Bragg Condition

To achieve high reflectivity in VCSELs, gratings consist of periodic layers with alternating index variations constitute the reflecting mirrors to produce a significant reflection at a particular wavelength called the “Bragg wavelength”. The period of the gratings is half of the optical path length and many small reflections at the interfaces add up in phase results in a large net reflection at Bragg wavelength so called the Bragg condition. In VCSELs, two quarter-wavelength thick layers with low and high indices constitute the element of the period and form the periodic stacks on one or both sides of the VCSEL during

epitaxial growth.

At a single interface the reflection coefficient for normal incidence is given by

$$r = \frac{n_1 - n_2}{n_1 + n_2}, \tag{2.11}$$

where n represents the refractive index. At Bragg condition, we suppose there exits only two indices n_1, n_2 in the alternating layers and no loss or gain in the medium, using the normal amplitudes of the incident and reflected electric fields in definition through a transmission matrix approach, the total reflection coefficient obtained from the gratings at Bragg wavelength is given by

$$r_g = \frac{1-(\frac{n_1}{n_2})^{2m}}{1+(\frac{n_1}{n_2})^{2m}}, \tag{2.12}$$

where m represents the number of the identical periods [11]. As we increase the number of periods m or the index difference between two materials, $\Delta n = n_1 - n_2$, the peak wavelength in the reflectivity spectrum broadens known as the stop band. The spectral width of this band is expressed as

$$\Delta\lambda = \frac{2\lambda_{Bragg}\Delta n}{\pi \cdot n_{eff}}, \tag{2.13}$$

where n_{eff} is the effective index of the mirror that has the same optical length normal to the layers in the DBR [12].

For the real DBR structures in VCSELs, the incident and exit medium may have different indices and the comprising layers may have more than just two materials, so the general form can be expressed as

$$r_g = \frac{1-b}{1+b} \quad \text{where} \quad b = \prod_{1}^{2m} \frac{n_O}{n_I} \cdot \frac{n_{Li}}{n_{Hi}}. \tag{2.14}$$

n_{Li} and n_{Hi} represent the low and high indices between the i th interface and n_I , n_O are the indices of the incident and transmitted medium [13].

2.2.2 *Design of DBRs*

To have high reflectivity and wide stop band for DBRs in VCSELs, large index contrast and more periods are needed. The dielectric stack deposited after the epitaxial growth is possible to have such property with a small number of the DBR periods. For instance the $ZnSe/CaF_2$ system produces greater than 99% reflectivity with only five periods of the DBR [14] and through the selective oxidation of AlAs, the $Al_2O_3/GaAs$ mirror performs as well for even fewer periods [15]. Despite the advantages of dielectric mirrors for high reflectivity, another deposition step on semiconductor active regions and the intracavity electrical contacts required for current injection make complexities to fabrication process.

Establishing monolithic semiconductor DBRs directly during epitaxial growth simplifies the VCSEL process and allows current injection throughout the mirrors. With lower index contrast and narrower stop band in comparison to those for the dielectric stack, semiconductor DBRs usually require more than 20 periods for GaAs/AlAs systems. Also to maximize the index difference between the adjacent mediums results in large energy band offsets and discontinuities with potential barriers that may cause high series resistance for the current flow. Thus compositional grading at the interfaces between the mirror layers and carefully controlled doping profiles at those interfaces where the optical field is at maximum effectively reduce the series resistance and prevent from ohmic heating that may decrease the laser performance [16,17]. The fabrication of DBRs through metalorganic vapor-phase epitaxy (MOVPE) with the ease of continuous compositional grading and the ease of doping with C as a p-type dopant which is more activated than Be make MOVPE an appropriate platform for VCSEL manufacturing.

2.3 *Optical Cavities*

With high-reflective DBR mirrors on both sides of a VCSEL, an optical cavity in the

middle is usually a single-wavelength thick and contains the active medium that provides gain. The optical cavity is intrinsic or lightly doped and is located at the p-n junction of the diode laser between two doped mirrors. The active medium in the optical cavity is commonly composed of several quantum wells that confine the carriers for optical recombinations to the gain process (Fig.2.3).

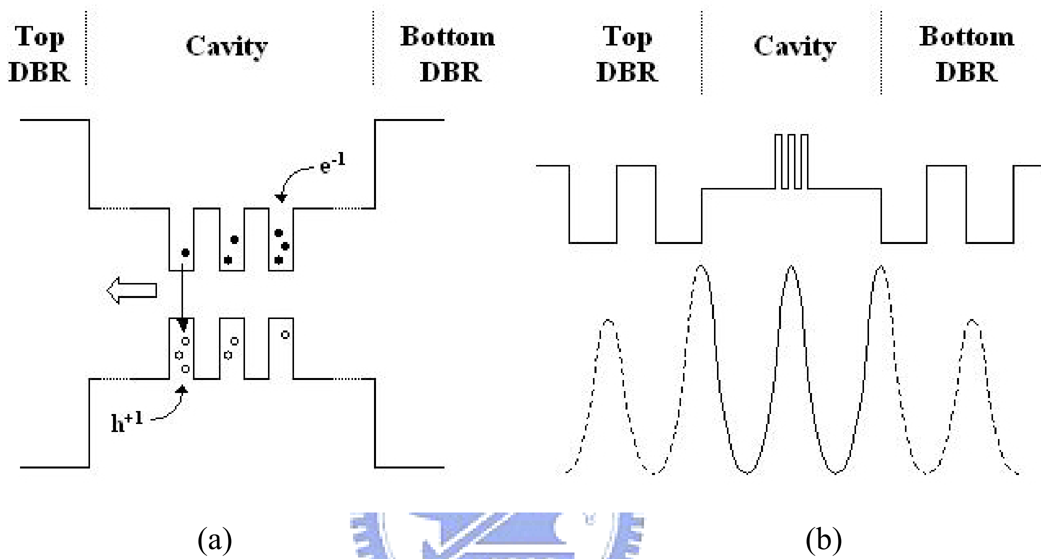

Fig. 2.3 The (a) heterostructure and (b) the optical field distribution in the cavity

2.3.1 Gain in Active Region

The definition of gain is mentioned before and the relation between the gain to energy or wavelength can be found through Einstein's approach to assume the two-level transition in the conduction and valance bands of the active region. The gain is expressed as

$$g_{21} = \frac{A_{21}}{\rho_0(\nu_{21})}\frac{h}{v_g}\rho_r(E_{21})(f_2 - f_1), \tag{2.15}$$

where the subscripts 2 and 1 represent the transition levels, A Einstein's coefficient, ρ_0 the optical mode density, ρ_r the reduced density of state, and f represents the quasi-Fermi level.

The above approximation is the form for bulk materials. The actual gain medium in

VCSELs is quantum-well structure and the formation of gain is far complicated. With consideration of dipole interactions between the optical fields and electron-hole pairs through the Schrodinger's equation, the gain in the material is given by

$$g_{21} = \frac{\pi q^2 \hbar}{n \varepsilon_0 c m_0^{\ 2}} \frac{1}{h \nu_{21}} \left| M_T(E_{21}) \right|^2 \rho_r(E_{21})(f_2 - f_1), \tag{2.16}$$

where $\left| M_T(E_{21}) \right|^2$ is referred as the transition matrix element and is related to the Hamiltonian with perturbation that the electromagnetic field modifies the charged carriers. Also with different transitions as the distinction of heavy holes and light holes and different polarizations of the field, $\left| M_T(E_{21}) \right|^2$ has different magnitude in each case. In quantum wells the transitions can be performed in any two quantized subbands, so the total gain at E_{21} is summed by all possible transitions,

$$g_{21} = \sum_{n_c} \sum_{n_v} g_{21}^{sub}(n_c, n_v), \tag{2.17}$$

where n_c and n_v represent the principal numbers in the conduction and valance bands. The gain for $n_c = n_v = 1$ is usually the largest that most transitions involved in the active region [9].

2.3.2 Design of Optical Cavities

The quantum well as the gain medium is usually less than 10nm for carrier confinement and with the surrounded claddings that makes up the one-wavelength thick optical cavity. For the one-wavelength thickness, there exits only one antinode of the optical field and its placement regarded to the center of the active medium has significant effects to the axial confinement factor for the short cavity length comparable to the wavelength as we mentioned before. So to place the antinode of the field centered at the quantum wells, for the limitation of space, there typically exits three quantum wells as the active region to compromise the increase in gain length and the reduction in confinement factor for optimization [18]. Another

subject of the optical cavity is to introduce compressive strain to the active quantum wells. The strain can change the curvature of the lowest energy hole band and produce high gain for the quantum wells leading to low threshold currents and high efficiencies in VCSELs [19].

2.4 Various Types of VCSELs

The longitudinal structure of a VCSEL has been described in the use of DBRs and active quantum wells for current injection and other optical properties. Lateral electrical and optical confinements are needed for individual devices and with various fabrication techniques, plenty of types of VCSELs have demonstrated. The typical forms often seen by former researches include the etched-pillar, etched/regrown, ion-implanted and the selectively oxidized VCSELs. The basic properties of those different types of VCSELs are as follows.

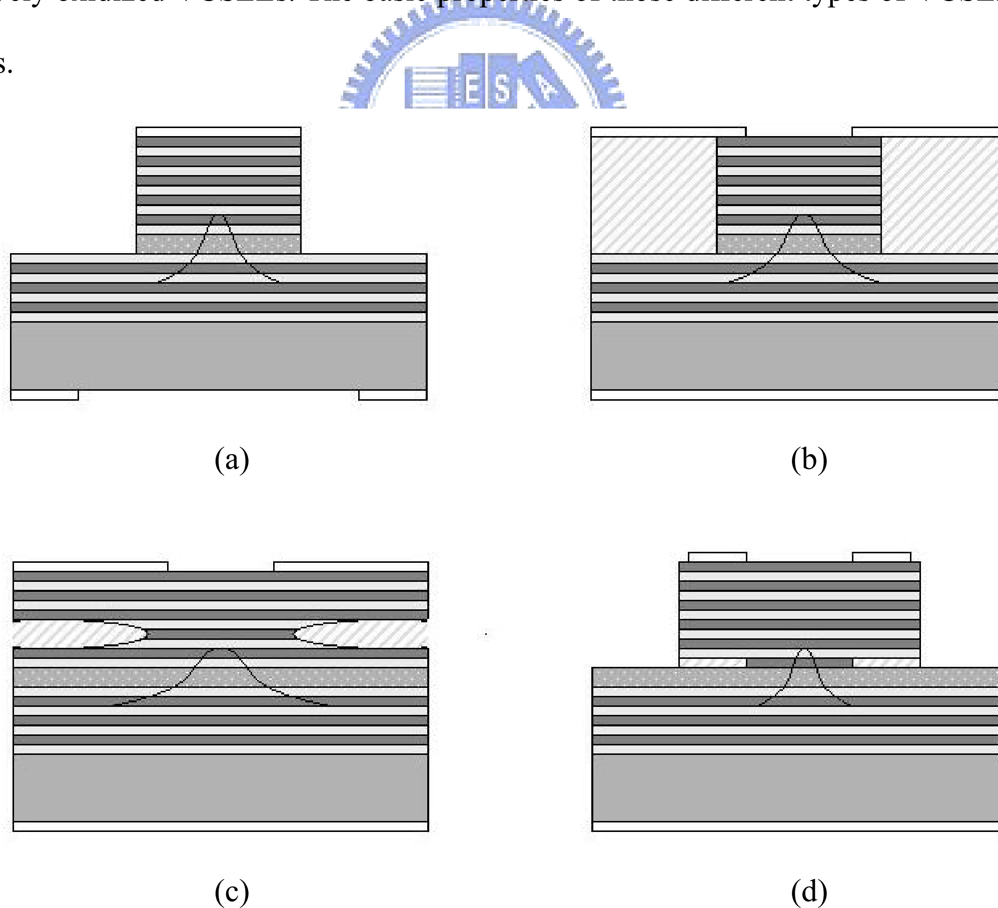

Fig. 2.4 The structures of (a) etched-pillar, (b) etched/regrown, (c) ion-implanted, (d) selectively oxidized VCSELs

2.4.1 *Etched-Pillar VCSELs*

To etch a pillar and transversely define the cavity is intuitional through the etching techniques. To remove the epitaxial material around the cavity through wet etching produces an isotropic etching profile. The unpredictable undercut edge profile and the difficulties to accomplish small pillar size make several limitations to the process control. Another anisotropic dry etching technique such as reactive ion etching (RIE), is able to achieve small diameter size thus reduces the active volume results in low threshold current and the smooth sidewall is achievable to decrease the optical loss. With small-diameter pillars from the use of dry etching, sub-milliamp threshold currents have been demonstrated [20]. The large index difference between the air and the semiconductor interface around the cavity provides strong index guiding to the laser waveguide.

The etch depths of the pillars can be classified to the shallow-etched depth to the top DBR mirror and the deep-etched depth throughout the active region. In the shallow pillar, the loss is attributed to the optical diffraction due to the axial index variation and the current spreading away from the active region contributes to loss. In the deep pillar the diffraction loss may be less affective for which the pillar is surrounded by air mostly, but the nonradiative recombination due to the high surface recombination velocity at the exposed sidewall of the active region may have significant contribution to loss. The roughness of the sidewall whatever in shallow or deep pillars can produce optical scattering loss.

Another important factor of the etched-pillar VCSELs is the thermal property relative to the roll over of output power. The heat sink material is removed from the laser cavity around thus the reduced thermal dissipation leads to high thermal impedance which has a dramatic impact on laser performance.

2.4.2 *Etched/Regrown VCSELs*

To deposit other semiconductor materials after etching a pillar also provides index

guiding effect with a lower refractive index material selected around or another higher index material to form the anti-guiding condition for special uses. The provided materials can also be chosen with higher bandgaps as the effective current blocks and the problem that affects the etched-pillar VCSELs for nonradiative recombinations can be released through the passivation on the sidewall of the active region. The regrown materials also provides good heat sinking that the device performance is much better than the etched-pillar case in terms of larger operating current range and higher output power [21].

The regrowth on highly reactive AlGaAs with high Al content inherent to the DBR mirrors makes difficulties to the process procedures. The fabrication methods include the dry etching with liquid phase epitaxy (LPE), the linked etching and molecular beam epitaxy (MBE) chambers with vacuum integrated, and the combination of dry and wet etching followed by MOVPE regrowth. The third way is considered the most applicable and has an advantage of selective regrowth to prevent from the deposition on the dielectric hard masks used for etching. In spite of the improvements in performance compared to the etched-pillar VCSELs, the complex fabrication techniques involving special cleaning, etching, and avoidance of exposure before regrowth are still considered expensive to the manufacturing area.

2.4.3 Ion-Implanted VCSELs

To define the transverse confinement in the planar structure, ion implantation has been widely used for the VCSEL fabrication. Ions projected into the top DBR mirror provides a nonconductive region for current impeding above the laser cavity. The ion implantation produces crystal vacancies to compensate the free carriers in a result of high resistive area for current confinement. The mostly used ion specie is proton and the implant energy defines the implantation depth. The density of vacancy provided by ions in the mirror stack has the peak value occurs typically at the position above the active region to prevent from damaging to the

active quantum wells and to reduce the lateral current spreading [22].

The mask against the ion implants can be used as photoresist or metals. During implantation, the wafer sample is usually angled by 7 ^{o} from normal to the incident ion beams which produce shallow depths to the periphery of the defined perimeter to perform better current confinement.

2.4.4 Selectively Oxidized VCSELs

To establish a lateral material difference of higher bandgaps for current confinement and lower index for optical guiding such as the etch/regrowth technique, another important innovation is to provide selective wet oxidation to the buried layers in the mirror stack [23]. The layers to be oxidized are buried in the top DBR mirror through the epitaxial growth by MOVPE for the ease of compositional control of monolithic semiconductor DBRs in AlGaAs system. The oxidation rate is sensitively affected by the composition of the $Al_xGa_{1-x}As$ layer thus we can specify a particular layer adjacent above the cavity to be oxidized more rapidly to form the current/optical confinement. The first step is to etch a mesa or an array of holes into the structure by dry etching techniques such as RIE, and expose these layers to water vapor which is transported in an inert gas such as nitrogen in an elevated temperature environment. The inert gas is controlled by a mass flow controller to a water bubbler bathed at a constant temperature and thus the water steam is carried by the gas flow into the preheated tube furnace where the samples take place of. To establish a stable and reproducible wet oxidation process requires careful control of the above relating process parameters and the identities of the layers themselves can tremendously affect the oxidation results [24].

The nonconductivity and the lower index of the oxide layer provide both electrical and optical confinements without damages in the mirror caused by implantation and no surface recombination problems at the sidewall. The oxide-confined VCSELs with prior performance

to other types of VCSELs soon arise with much attention to the VCSEL technology.

Chapter 3

Experiment

The experiment is to fabricate the planar ion-implanted VCSELs and to perform wafer-level testing of those devices. We designed various aperture sizes for current confinement by ion implantation and the top metal contact openings for light output through. The purpose of the experiment is to compare the electrical and optical characteristics of various structured-VCSELs and to figure out the possible reasons of those results.

The layer structure of the wafer we used has not much difference to the former designed VCSEL structures. It contains a 23-pair p-doped (C) quarter-wave $Al_{0.9}Ga_{0.1}As/Al_{0.12}Ga_{0.88}As$ stacks as the top DBR, three GaAs quantum wells as the active region centered in the one-wave cavity spacer and a 34.5-pair n-doped (Si) quarter-wave $Al_{0.9}Ga_{0.1}As/Al_{0.12}Ga_{0.88}As$ stacks as the bottom DBR grown on an n^+-GaAs substrate. The composition grading of the DBRs and the spacer is also implemented.

The fabrication process was performed with three photolithographic procedures (masks). The detailed process steps are listed at the end of this chapter and here we just describe it briefly. First we deposited SiO_2 on the wafer using plasma enhanced chemical vapor deposition (PECVD), then a lithographic process was performed to define the pattern and then the SiO_2 was etched by reactive ion etching (RIE). Second, another lithographic process was performed to define the un-implanted region ready for ion implantation. The third lithographic process defined the pattern of the metal layer with rings and pads at the same time. The p-metal evaporation with an e-gun and the annealing process to both the metal/semiconductor interface and the implanted area was performed. After that the n-metal evaporation on the back side of the wafer was followed by the general lapping and polishing procedures and finally another annealing process for n-metal was also applied. A brief sketch

of the whole process is shown in Fig. 3.1.

The different implant and contact aperture sizes are from 12 to 6 um and 12 to 4 um in diameters, respectively, separated by 2 um. We assume that the real aperture sizes of those devices are approximately the same to the patterns defined by the masks.

The device testing was directly performed on the wafer with the bottom placed on a conductive stage as the negative side and a probe on the pad of the device as the positive side. We used a current source, a voltage meter, and an optical power meter directly above the contact opening to have the diode voltage and output power as function of the injection current and used a multimode fiber to conduct the output light toward a spectrometer to get the emission spectrum at different bias currents. All measurements were performed under continuous- wave operation at room temperature.

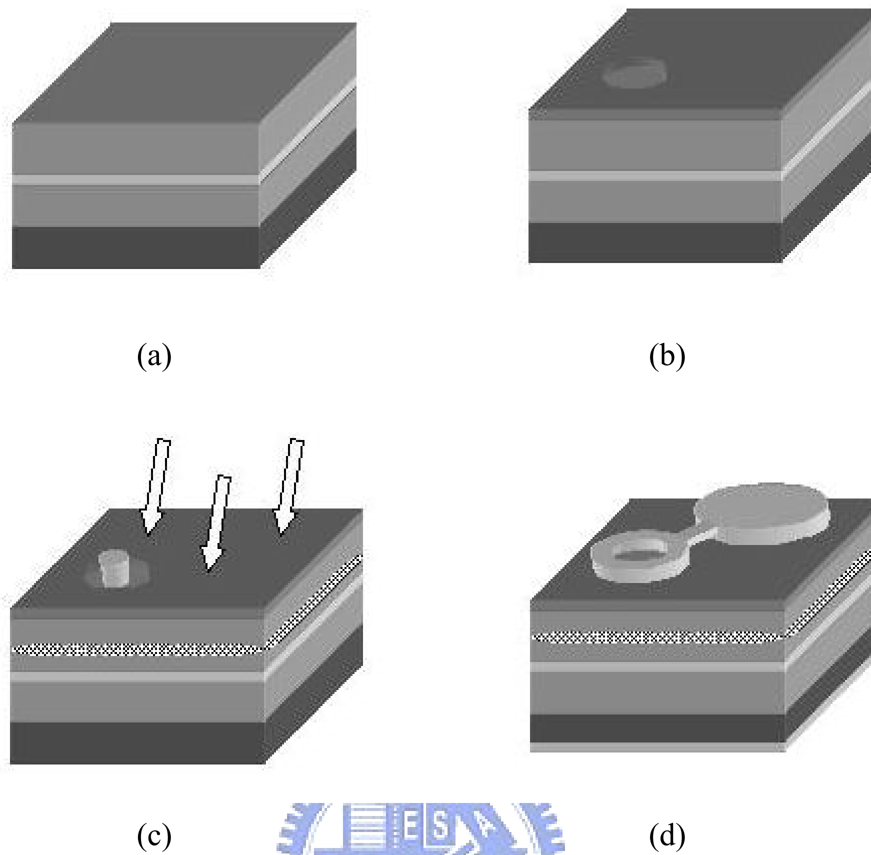

Fig. 3.1 The process procedures of the device with the (a) original wafer, (b) SiO_2 deposition, (c) ion implantation, and (d) metal evaporation

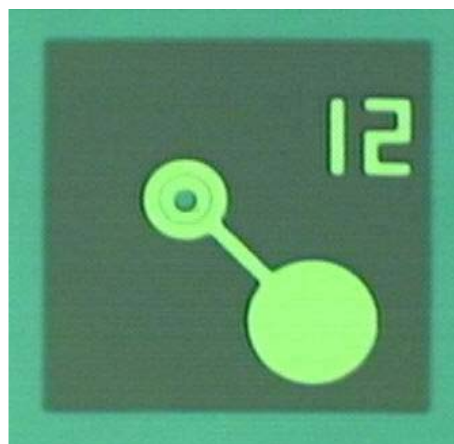

Fig. 3.2 The top view image of the device

More Specific Process Steps :

1 .

Wafer Clean	:	ACE(Acetone) , IPA(Isopropyalcohol) , B.O.E 5’
SiO_2 Deposition	:	PECVD 1000A / 3500A
Lithography	:	Baking 120 ^oC 5’ Photoresist 500rpm 5” , 3500rpm 25” Baking 100 ^oC 1’ Exposure 4” Baking 120 ^oC 2’ Exposure 35” Develop 40” Baking 120 ^oC 10’
SiO_2 Etching	:	RIE
Remove PR	:	ACE 5’ , IPA 2’

2.

Lithography	:	Baking 120 ^oC 5’ Photoresist 1000rpm 3” , 4000rpm 35” Baking 120 ^oC 5’ Exposure 17” Develop 3’ Baking 120 ^oC 10’
Implantation	:	H^+ 10^{15} cm^{-2} 200 keV
Remove PR	:	ACE 5’ , IPA 2’ , H_2SO_4 3’ (heating)

3.

Lithography : Baking 120 ^{o}C 5’
Photoresist 500rpm 5” , 3500rpm 25”
Baking 100 ^{o}C 1’
Exposure 4”
Baking 120 ^{o}C 2’
Exposure 35”
Develop 40”
Baking 120 ^{o}C 10’

Clean : CH_3COOH / NH_4F/H_2O 1’

Evaporation : Ti / Pt / Au ~ 9000A

Annealing : 420 ^{o}C 5’

4.

PR Protection : Photoresist 1000rpm 3” , 4000rpm 35”
Baking 120 ^{o}C 10’

Lapping / Polishing

Evaporation : AuGe / Ni / Au ~ 4000A

Remove PR : ACE 10’ (heating) , IPA 5’

Annealing : 420 ^{o}C 5’

Chapter 4

Result and Discussion

The VCSEL device fabrication and characterization were performed as listed in chapter 3. In this chapter, we further analyze the measurement results in many aspects and give the underlying theoretical explanation. We separate the experiments with results into four parts. In the first section, we studied the effects of implantation depth and its influence on the device characteristics by varying the thickness of hard mask SiO_2. In the second part, we investigated the voltage-current characteristics of VCSELs with various implant and contact aperture along with the series resistance consideration. The light power/current relation denotes the characteristics of threshold current (density), peak power, and operating current range relative to thermal properties. In the third section, the general behavior of emission spectrum for implanted VCSELs is covered. Finally, in the primarily part of the results, we analyze the slope efficiencies in L-I curves in relation to the transverse mode formation of implanted VCSELs and discover their influence on the devices with different apertures especially for the implant apertures.

4.1 Ion Implantation

The main concern of the ion implantation is the ion penetration depth. It is the longitudinal distance from the surface to the place where the highest density of crystal vacancy produced by ion implants occurs, and is often referred as the mean projection range. In the real situation, the penetration depth can be larger or smaller than the mean projection-range value. The density of vacancy/ion is in a Gaussian form along the vertical axes with a deviation called straggling, which denotes a relative high dense area of the damage caused by

the implants.

The SiO_2 deposition before ion implantation process results in different ion projection ranges in the DBR stack with or without the masked SiO_2 layer. The thickness of SiO_2 were selected for about 1000 A and 3500 A for comparison purpose. Using TRIM-98 to estimate the ion distribution profile for the devices with different SiO_2 thickness and the non-deposition situation and get the result shown in Fig. 4.1. Both three situations have approximately the same straggling about 0.16 um. The depths correspond to the peak values for the 1000 A-deposited and non-deposition cases are differed from about 0.1 um and for 3500 A the difference is about 0.33 um. It shows that the difference in depths between the non-deposition and 1000 A-deposited situations is still in the limited range of the straggling which reveals that the border between the regions with different projection range still remains a high dense area of implants. The difference in depth for 0.33 um is far away from the value of the straggling thus the serious discontinuity of ion distribution may cause disadvantages for current confinement.

The devices with different SiO_2 thickness both work and their output characteristics are shown in Fig. 4.2. The discontinuous distribution of implant dosage may cause more leakage current to alleviate the current confinement effect in a result of higher threshold current and seriously unstable output power with injection current in the device with 3500 A SiO_2. Another device with 1000 A SiO_2 performs generally as well as other typical implanted VCSELs. It shows that the relative shallow SiO_2 deposition before ion implantation with small difference on ion projection range has less effect to the current confinement and output characteristic in comparison to those of typical implanted VCSELs with metal contacts evaporated before ion implantation.

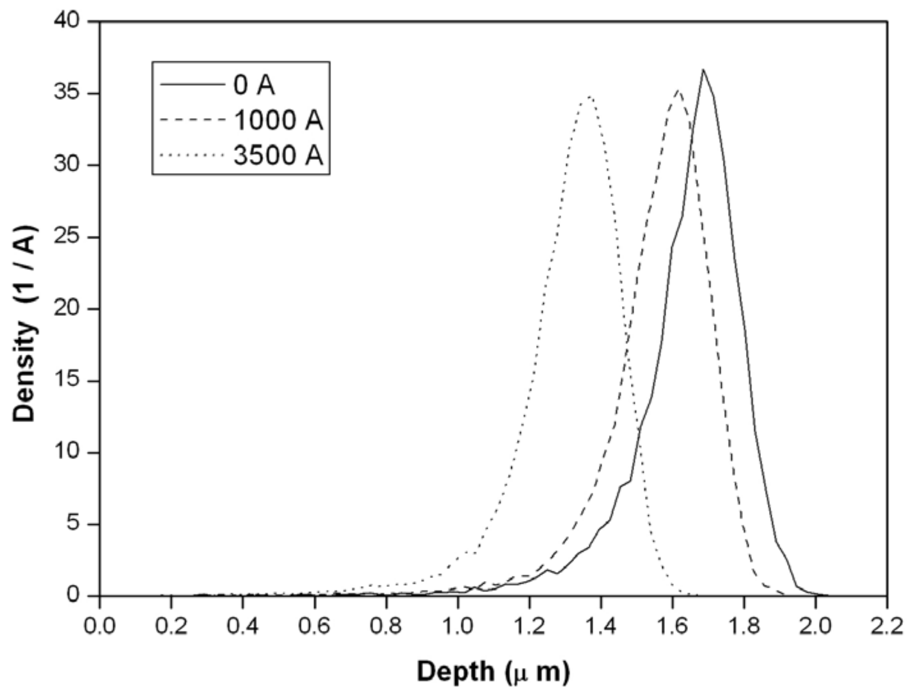

Fig. 4.1 The simulated ion-implantation profile of the devices with different SiO_2 thickness

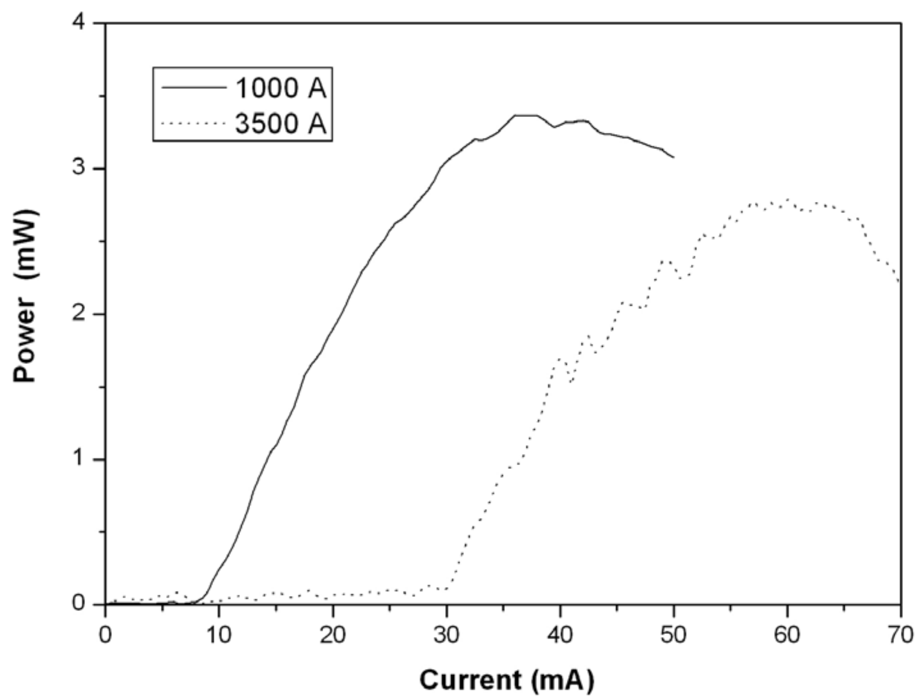

Fig. 4.2 The output characteristics of the devices with different SiO_2 thickness

4.2 L-I-V Characteristics

From now on, the implant and contact aperture relations are concerned and all devices we discussed are with 1000 A SiO_2. The device with 12um of each aperture is set as the standard and the size variation of each aperture is considered with the other one fixed at 12 um. For example, the devices with various implant apertures from 12 to 6 um are all 12um for contact apertures and vice versa with contact apertures varying from 12 to 4 um. The following analysis is of this rule when some kind of the aperture variation is mentioned without further explanation for simplicity.

The I-V characteristics are shown in Fig. 4.3, Fig. 4.4 and the series resistance of each device is calculated from threshold to 30 mA using a simple linear regression method and can be seen in Fig. 4.5. The increasing resistance for the devices with decreasing implant apertures shows the result of the impeded current flow. For the contact aperture variation the resistance is almost the same implies that the area of the current passage in the top DBR stack dominates the resistance problem, in stead of the metal contact distribution on the surface.

The L-I characteristics are shown in Fig. 4.6, Fig. 4.7, and the threshold current (density) of each device is in Fig. 4.8. Assume the current passes through the un-implanted region and spreads out to form a Gaussian-type distribution of current with respect to the horizontal plane in the cavity, and from (2.10) we can accept that the gain distribution in the active region is approximately proportional to the current/carrier density distribution bellow threshold. The gain is higher in the device with smaller implant aperture due to the smaller excitation area in the active region and the threshold condition is reached at lower current. The threshold current dependence on contact aperture size is the same tendency but is less variant in degree compared to the dependence on implant aperture size. Without the direct influence on current density from the area of the current passage, lateral current spreading

from the contact stripe plays the role. The current leaving the edge of the stripe spreads away into the DBR stack with an exponential decay of current density with respect to the lateral distance [25]. The smaller contact aperture produces relative higher current density/gain in the middle of the active region with threshold condition at lower bias.

The output power increases with injection current but starts to decrease with a peak value for each device. This power roll over is due to the thermal effect caused by the heating of the resistive current path and the increasing light generation in the active region. The thermal dependence of energy gap and Fermi levels has great influence on the gain spectrum with the gain peak shifting to a longer wavelength at higher temperature/current. Also the cavity resonance wavelength does the same cause of the change in refractive index with temperature in the DBR mirrors and the cavity, $n(Al_xGa_{1-x}As) = n_{x=0} + 3\times10^{-4}\cdot x\cdot\Delta T$ [26]. The gain peak moves faster than the resonance wavelength along with the injection current results in mismatch thus the decrease of output power (Fig.4.9).

The current range from threshold to the value with maximum light output and the peak power for each device are shown in Fig. 4.10 and Fig. 4.11. The current range for the device with smaller implant aperture reduces because the higher current density and intensity of light in the active region with sufficient heating effect make up the roll-over condition with less additional injection current above threshold. The decreasing peak power can be explain by the lower current with less carrier participation to photon generation. The peak power for the device with smaller contact aperture decreases more obviously is not because of the more current/carrier contribution to light due to the less degree of reduction in current range. It is for the contact area that directly impedes the output light. The decreasing current range can be explained by the heating effect with more light restricted inside below the metal area in the device with smaller contact opening.

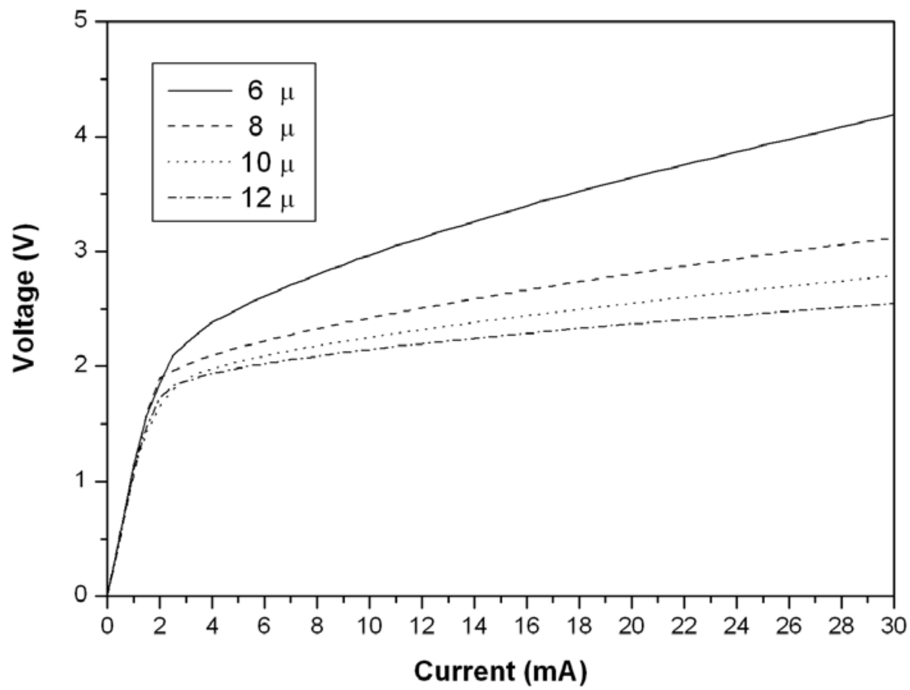

Fig. 4.3 The I-V characteristics of the devices with different implant aperture sizes

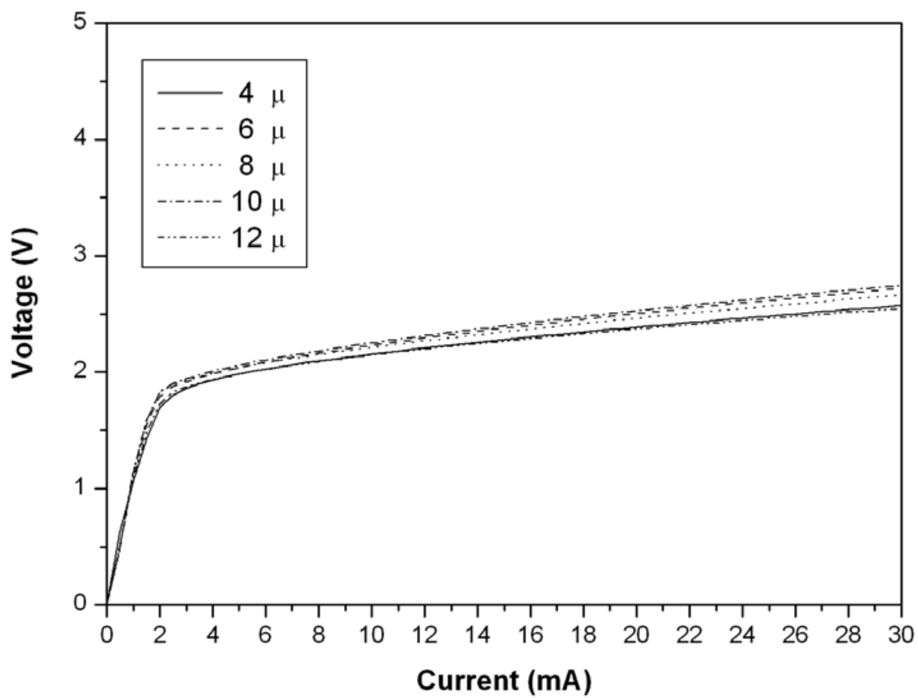

Fig. 4.4 The I-V characteristics of the devices with different contact aperture sizes

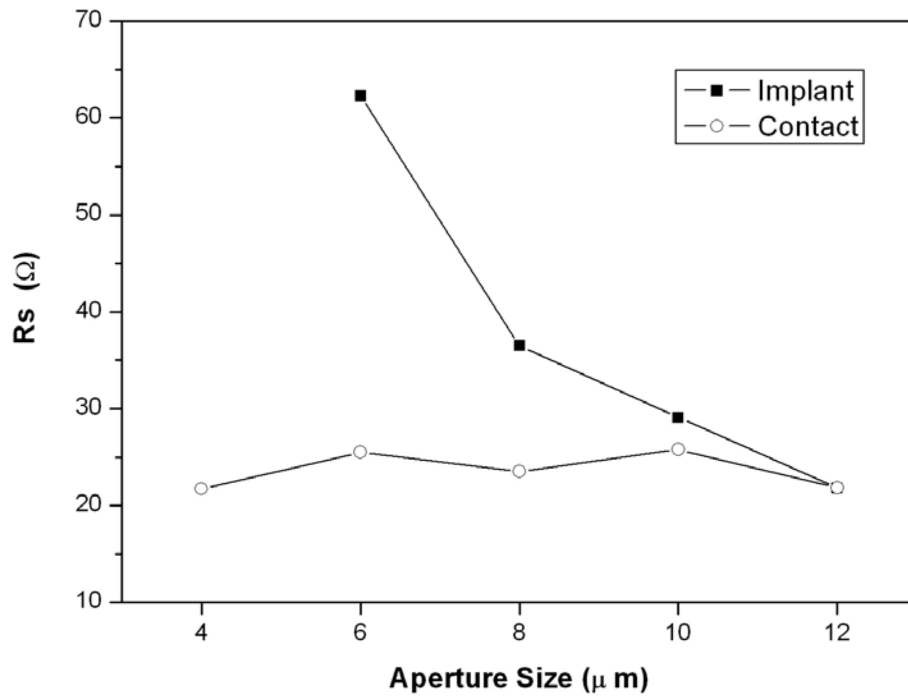

Fig. 4.5 The series resistance of the devices with different aperture sizes

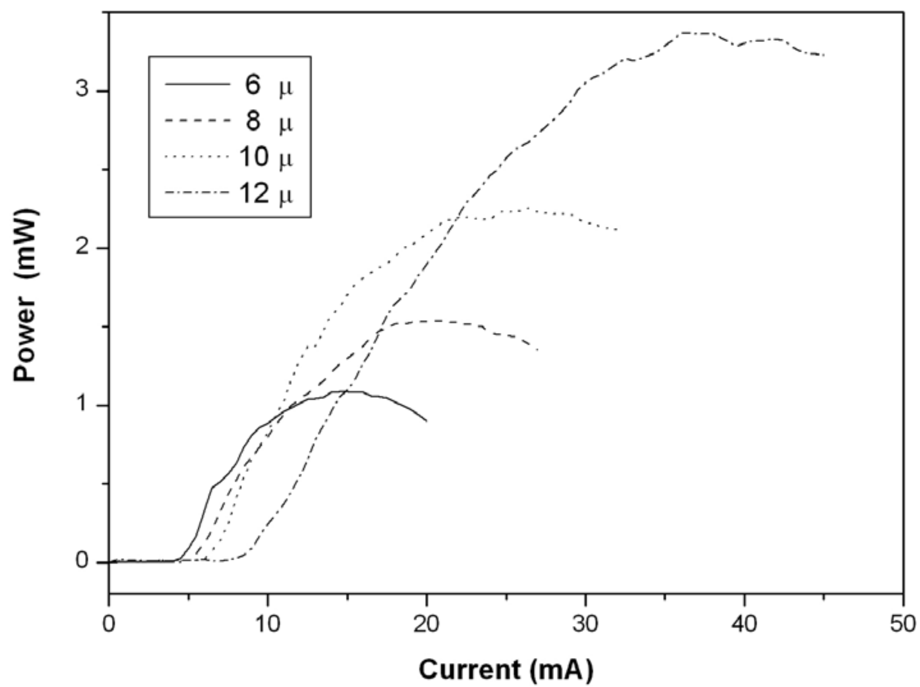

Fig. 4.6 The L-I characteristics of the devices with different implant aperture sizes

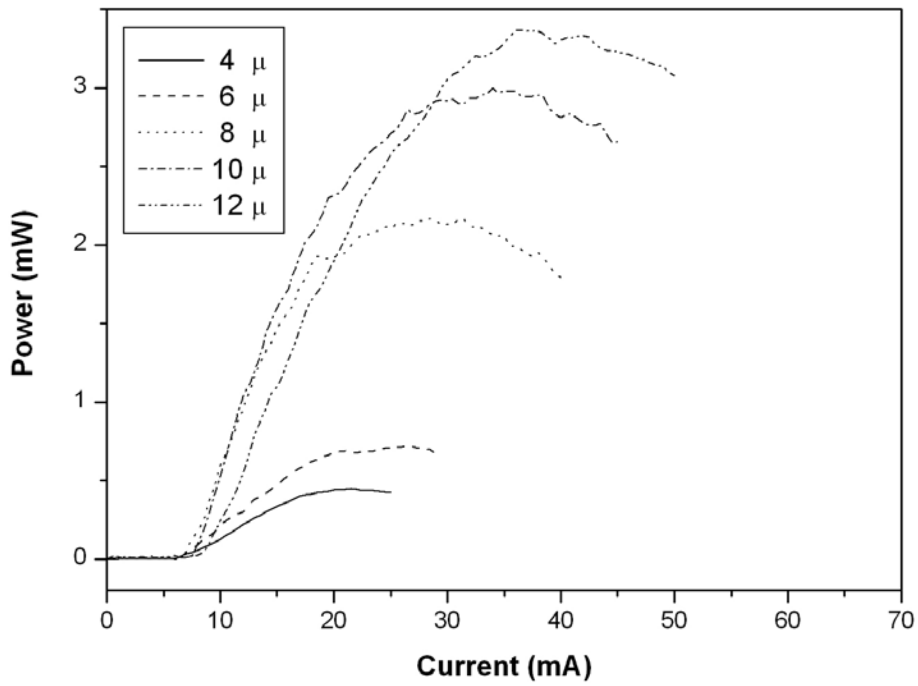

Fig. 4.7 The L-I characteristics of the devices with different contact aperture sizes

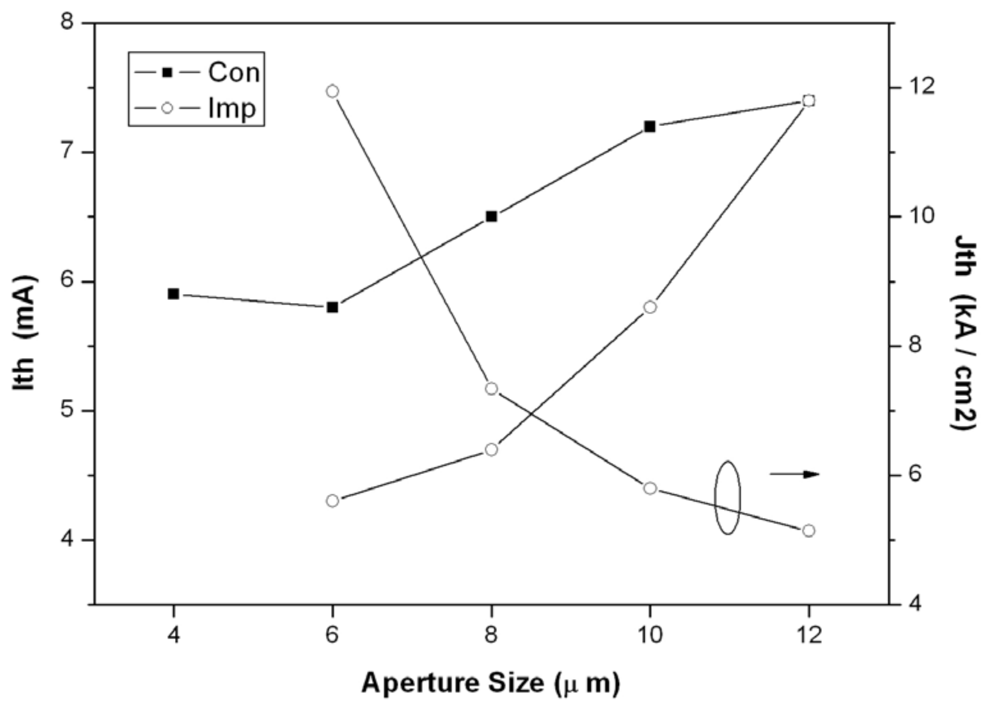

Fig. 4.8 The threshold current (density) of the devices with different aperture sizes

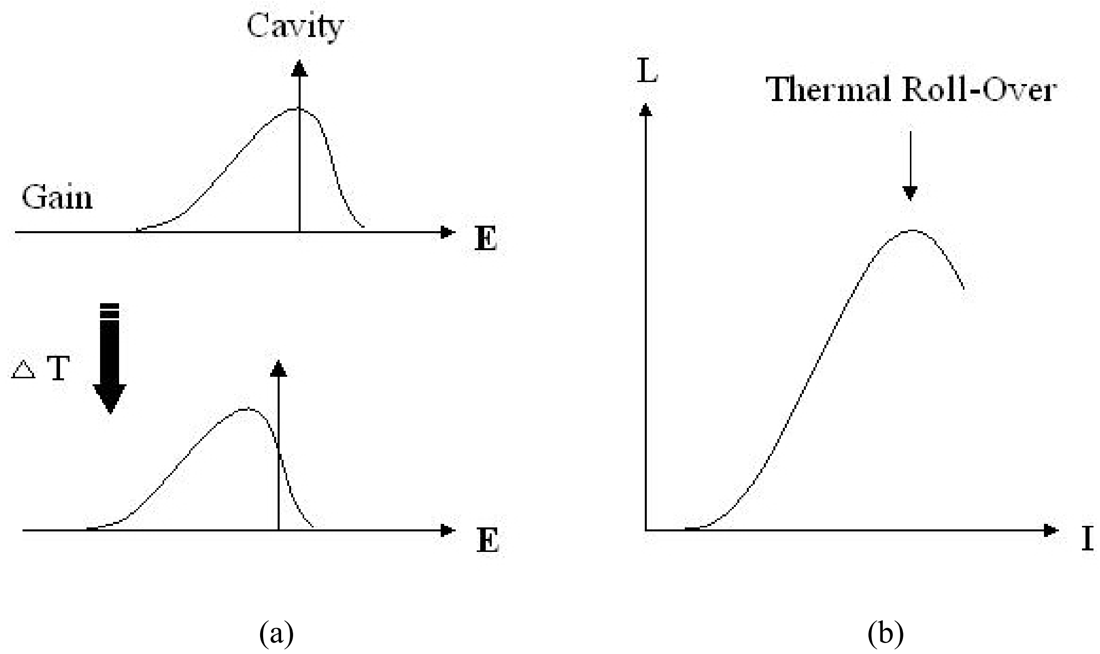

Fig. 4.9 (a) The gain/cavity mismatch and (b) the thermal roll over effect

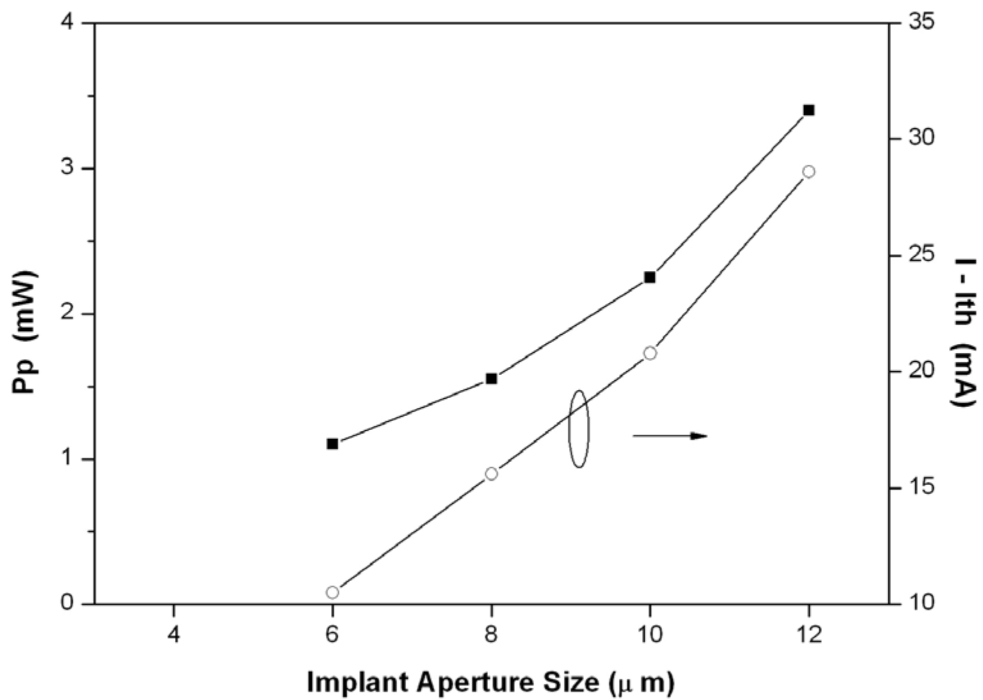

Fig. 4.10 The peak power and current range of the devices with different implant aperture sizes

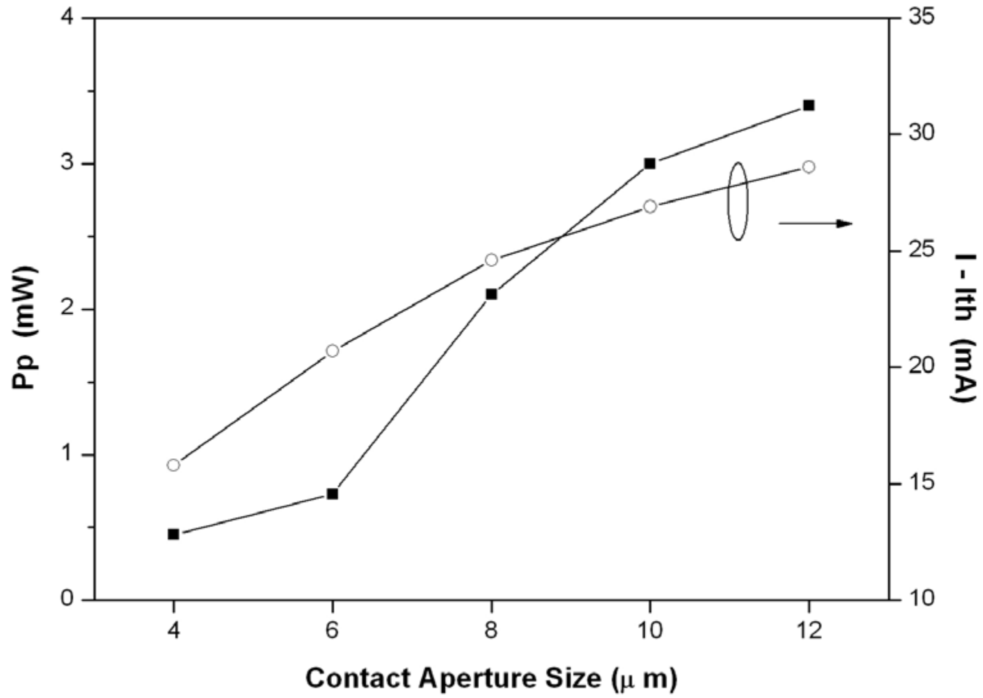

Fig. 4.11 The peak power and current range of the devices with different contact aperture sizes

4.3 Emission Spectrum

The general behavior of emission spectrum for implanted VCSELs is shown in Fig. 4.12. With additional injection current, the number of peaks in wavelength of the spectrum increases due to the numerous transverse modes formation. The peak wavelengths shift to be longer as the bias current increases in consequence of the thermal dependence on energy gap of the gain medium,

$$Eg(GaAs) = 1.519 - \frac{5.405 \times 10^{-4} T^2}{T + 204} (eV) \quad [27]. \tag{4.1}$$

The quantity of the red shift also becomes larger at higher currents with more heating effect and can be verified by the square term of temperature in the numerator. From the L-I curve the slope gradually decreases toward roll over condition and supposing that the power dissipation $P_{IV} - P_{h\nu}$ all contributes to heat, the enhanced red shift with constant additional

injection at higher current is reasonable.

The individual transverse mode profile can be calculated using the diffraction integral formula with the solution of Hermite-Gaussian distribution of the optical field [28]. The fundamental mode forms at the center while the other higher order modes arise in the periphery. The formation of various transverse modes in VCSELs is primarily because of the refractive index variation that results in different guided modes. Assume the index variation in the active region with x-y symmetry, $n^2(r) = n_0(1-g^2r^2)$, where n_0 is the index in the central region and g is a constant characteristic of the medium. The relation between two characteristic Hermite polynomials obtained from the solution of the wave equation is given by

$$\beta_{l,m} = k[1-\frac{2g}{k}(l+m+1)]^{1/2}. \quad (4.2)$$

$\beta_{l,m}$ is the propagation constant in the longitudinal direction, k is the wave number, and l, m are integers with larger numbers for higher order modes [29]. The index variation in implanted VCSELs is small and we assume that the fundamental and higher order modes have the same effective resonance wavelength along vertical axes according to the one-wavelength cavity. For constant β , the larger l, m for higher order modes implies the larger k and smaller λ with the relation, $\lambda = 2\pi \cdot n_0 k^{-1}$. This recognizes the result of the emission spectrum with more peaks at shorter wavelength due to more transverse mode generation along with the increasing injection current.

The situations $l+m=0$ and $l+m=1$ represent the fundamental TEM_{00} and the first order TEM_{01} modes, respectively. We can roughly estimate the wavelength spacing between these two adjacent modes with $n_0 = 3.4$, $\beta = 2\pi \cdot n_0 \lambda^{-1}$, $\lambda = 0.85 \mu m$, $g \approx 2\times10^{-2} \mu m^{-1}$, [30] and get the result of nearly 1 A. The other experiment has shown that this wavelength spacing at threshold bias is about 2 A for implanted VCSELs [31]. The wavelength spacing is

so small that the peaks of the spectrum in Fig. 4.12 are definitely not representative of any order mode respectively. The spectrum at 8 mA (Ith = 5.8 mA) is not a single mode condition due to the $FWHM \cong 5A$ and should be considered as the superposition of lower order modes.

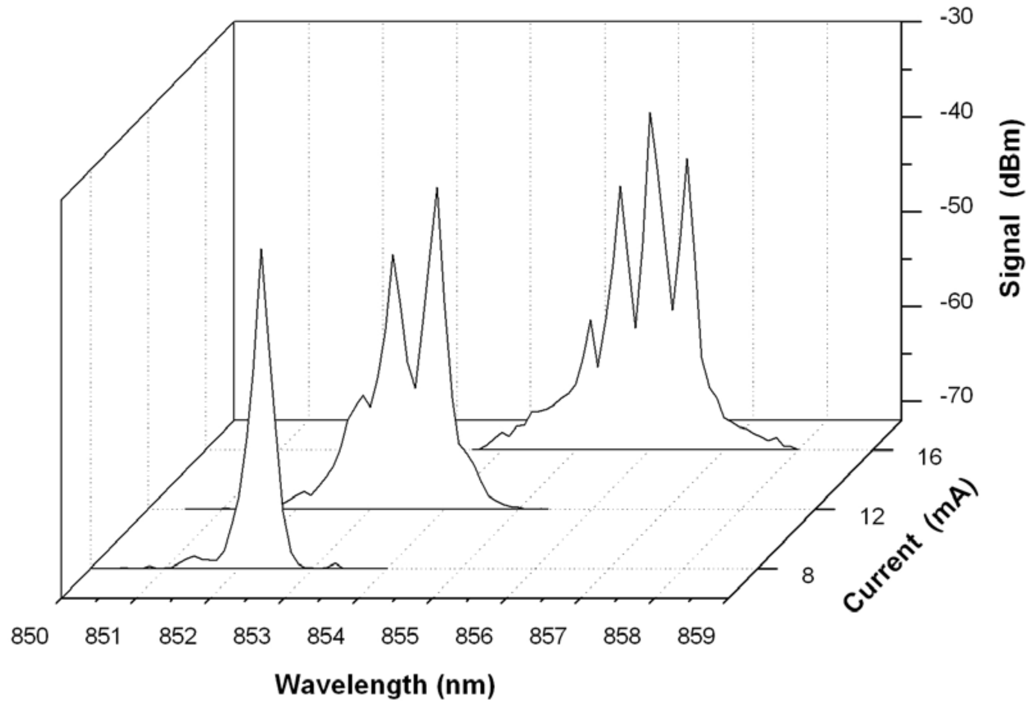

Fig. 4.12 The emission spectrum of the implanted VCSEL

4.4 Slope Efficiencies in L-I Curves

4.4.1 Gain and Index Guiding

The optical guiding of VCSELs is generally discriminated between the gain guiding and index guiding (Fig.4.13). The implanted VCSELs are regarded as gain-guided for the reason that the spatial distribution of gain originated from the current spreading as we mentioned in section 4.2, restricts the area of light generation where the gain is above threshold. The damage caused by ion implantation in the top mirror is nearly invariant in refractive index

and does not affect the output light. The oxidized VCSELs are typically index-guided with a large refractive index step between the semiconductor and the oxide layer with $Al_{0.98}Ga_{0.02}As$ $(n_r \cong 3.0)$ and Al_2O_3 $(n_r \cong 1.6)$, respectively. The oxide layer serves as both the current and optical confinement and is adjacent above the cavity with least current spreading. The reduced current spreading results in uniform distribution of gain in the active region with a lower threshold current. Besides, plenty of the transverse modes obtain sufficient gain in the middle and periphery of the active region and arise at the same time slightly above threshold. Because of the multimode condition at relative small bias above threshold, the single mode operation range is small and so are the fundamental mode size and power due to the transverse mode competition. The refractive index step formed by the oxide layer can be considered as a small waveguide similar to the indexed-fiber with its multimode behavior [32].

4.4.2 Spatial Hole Burning and Self-Focusing Effects

The formation of higher order modes in implanted VCSELs is due to the spatial distribution of gain and the hole burning effect above threshold. The light starts to create as the fundamental mode in the middle of the active region and as the mode power increases with injection current, the enhanced intensity of light accelerates the stimulated emission effect and contrarily reduces the carrier population in the middle of the area thus creates a spatial hole in the distribution of carriers/gain (Fig.4.14). With further increasing of the bias current, the gain in the surroundings continues to increase and eventually above threshold, thus the higher-order modes start to lase. This spatial hole burning effect has been observed in early experiments [33,34].

Beside the spatial hole burning, the index-guiding phenomenon due to the thermal dependence on refractive index in the active region for implanted VCSELs, dominates the multimode behavior at relative higher currents above threshold. The thermally-induced index

variation becomes more gradient as the bias current increases from threshold thus the fundamental mode is guided in a smaller area with larger intensity which aggravates the hole burning effect [35]. The relative lower carrier density in the spatial hole also contributes to index guiding for which the refractive index is inversely proportional to the carrier density. Although the increasing intensity of light, the self-focusing effect due to the progressive index grading reduces the mode size which results in the saturated output power with increasing bias current until the next higher order mode arises with additional power contribution. The mode size shrinkage and the formation of higher order modes cause nonlinear output power with injection current thus the kink phenomenon in the L-I curves (Fig.4.15).

4.4.3 Kink and Slope Efficiency

The kink phenomenon is more clearly observed from the slope efficiencies in the L-I curve at various current within the operation range. The spatial hole burning and self-focusing effects along with the formation of the higher order modes, and the antiguiding effect originated from the refractive index dependence on carrier density with higher index in the surroundings due to the hole burning effect of the higher order modes, are reasons for those kinks. As we can see in Fig. 4.16, the variation of the slope at higher currents is quite complicated but the fact that the slope increases regularly above threshold to a local maximum and suddenly drops at the place corresponding to the first kink does contain particular meanings. The process of this phenomenon can be explained that the light intensity of the fundamental mode increases continuously above threshold, then the power saturates noticed by the decreasing slope at the place of the kink due to mode shrinkage with self-focusing effect. After that, the slope turns to increase again from a local minimum value and it implies the generation of the first order mode with additional power contribution. Thus, we boldly regard the bias point at the first local minimum of slope efficiency as the

maximum single-mode condition.

The slope efficiency, power, and current range above threshold according to this bias point for the device with each implant aperture are shown in Fig. 4.17. The higher slope efficiency for the device with smaller implant aperture is reasonable for the higher current density in the active region. The decreasing current range implies that the temperature effect in the smaller device produces more refractive index grading for self-focusing effect with the first order mode arising at lower bias current. The lower power is because of the smaller mode size with more graded index and less carrier contribution to light due to the smaller operating current range.

We apply the same method and get those characters for the devices with different contact apertures in Fig. 4.18. We can imagine that in the device with smaller contact aperture, the higher-order modes should be suppressed in the periphery and a larger current range for single mode operation is expected. Unfortunately, the result in Fig. 4.18 doesn't conform to it. The reason for that is the bias point we chose for the kink position does not truly reflect the maximum single-mode condition as we described before. The statement on which this condition relies is useless here because the variance of slope efficiency is no longer simply affected by the spatial hole burning and self-focusing effects. The kink position we chose is possible in consequence of the power suppression of light by the metal contact as we see in Fig. 4.7 for the power reduction in the devices with smaller apertures.

To satisfy the expectation, we compare the characteristics of the emission spectrums between the devices with 12 and 4 um of the contact apertures. From the general behavior of emission spectrum for implanted VCSELs we discussed in (Fig.4.12), the increasing number of peaks from one, two and so forth indicates more and more higher-order modes involved. We recorded each current range and power according to the selected bias point for the two devices in Fig. 4.19 and Fig. 4.20. The emission spectrum for the device in Fig. 4.19 has a second peak with a value less than 20 dB in intensity in comparison with the value of the

original peak produced at threshold condition. The emission spectrum for the device in Fig. 4.20 has only a single peak without a second one comparable to it with less than 20 dB in intensity. This implies that the output of the device in Fig. 4.19 has more transverse modes than the output of the device in Fig. 4.20. Each recorded power is not the maximum single-mode power as we considered in the former case for the devices with various implant apertures, but it fairly represents the power of lower order modes. From these results, we can find out the agreement with the expectation that the contact layer with smaller aperture does extend the device operating current range for an output with lower order modes.

4.4.4 Fundamental Mode Size and Contact Apertures

The smaller contact opening retains the light output with approximately the same relative lower order modes compared to the larger one at higher injection current, and it is reasonable to produce a higher output power due to more injected carriers contribute to light power. But it is not exactly the way it goes from Fig. 4.19 and Fig. 4.20 with the reduced power for the 4-um device. The possible reason for that is the lower order modes, even the fundamental mode, is depressed by the contact opening at the beginning of the threshold condition or above. This can be observed in Fig. 4.7 especially for the smaller 4- and 6-um devices with noticeable power reduction.

Take the fundamental mode for instance, we estimate the mode size with an assumption of parabolic-decreased index variation in cylindrical symmetry within the active region, $n_r(r) = n_r(0) - \frac{\Delta n_r}{R^2} \cdot r^2$, where $n_r(0)$ is the index in the central region and Δn_r is the index change over a radius R. The Δn_r depends on the variation of carrier density and temperature with the spatial hole burning and thermal lens effects, respectively, and can be expressed as

$$\Delta n_r = \frac{\partial n_r}{\partial N} \Delta N + \frac{\partial n_r}{\partial T} \Delta T \quad , \tag{4.3}$$

where $\frac{\partial n_r}{\partial T} \approx 4 \times 10^{-4} K^{-1}$ [36]. To ignore the gain guiding $\frac{\partial n_r}{\partial N} \Delta N \approx 0$, we use the assumption $\varepsilon(r) = \varepsilon(0) - a^2 r^2$ to solve the wave equation $\nabla^2 E + \omega^2 \mu_0 \varepsilon \cdot E = 0$ and the intensity distribution of the fundamental mode is given by

$$|E(r)|^2 = \exp\left[-(a \cdot k_0 / \sqrt{\varepsilon_0}) \cdot r^2\right], \qquad (4.4)$$

where ε is the dielectric constant relative to the thermally-induced index change and a is a real constant. The ε and $n_r(r)$ can be related and finally the fundamental mode width is obtained in the form of

$$W = \left(\frac{4R\lambda}{\pi \cdot \sqrt{2n_r(0) \cdot \Delta n_r}}\right)^{1/2}, \qquad (4.5)$$

where λ is the emission wavelength and W is the diameter with e^{-2} of the field intensity of the fundamental mode [25]. Assume the power dissipation all contributes to heat and the heat source in the device is uniformly distributed along the vertical axes with the heat flows only in the horizontal plane. The temperature variance ΔT from the center to the edge of the active region is estimated through the Green's function and is given by

$$\Delta T = \frac{P_{IV} - P_{h\nu}}{2\pi \cdot d \cdot \sigma}, \qquad (4.6)$$

where $\sigma \approx 0.14 K^{-1} cm^{-1} W$ is the thermal conductivity and $d \approx 5\mu m$ is the total vertical thickness that $\Delta P = P_{IV} - P_{h\nu}$ dissipates [36,37]. Suppose that the temperature variance is mostly within the active region determined by the implant aperture and applying the formulas above to the device in Fig. 4.19 with $R = 6\mu m$, $\lambda = 0.85\mu m$, and $n_r(0) = 3.4$ at 8 mA (Ith = 7.4 mA) with the voltage (2.09V) and the output power (0.03W), the results are $\Delta T \approx 38^o C$ and $W \approx 4.5\mu m$.

The estimated fundamental mode width with 4.5 um larger than the 4-um contact opening satisfies the former possible reason we made that the depression of the fundamental mode at the beginning of the threshold and the remarkable power reduction in Fig. 4.7 are verified. In Fig. 4.7, the 6-um device also behaves similarly to the 4-um one with significant

power reduction compared to other devices with larger contact apertures. Although 6 um is larger than the estimated fundamental mode width, but the assumptions of those formulas are in the consideration with the implanted area slightly above the cavity with least current spreading. The implantation energy in regular process is often chosen as about 300 keV for typical implanted VCSEL structure with approximately 3 um in thickness of top DBR stack. The devices we have are 200 keV in energy with the implantation depth approximately half of the top DBR in thickness ($\approx 1.63\mu m$) as shown in Fig. 4.1. Thus, the relative serious current spreading results in over-estimated P_{IV} for more injection current and less-graded index variation Δn_r in the region with $R = 6\mu m$ in radius leads to a larger mode diameter W. The larger mode size may be comparable to the 6-um contact opening thus the similar power reduction as well as in the 4-um device is acceptable.

The slope variations of the L-I curves in these two devices are shown in Fig. 4.21 and Fig. 4.22. We can see that the device with smaller contact aperture not only extents the operating current range for the output with relative lower order modes, but also performs better with more linear output characteristic [38]. This can be observed by the fact that the slope of this device retains at a relative higher value for a large current range from threshold to roll over condition and the slope of the other one gradually decays immediately from the maximum value near threshold during the operation range. This also verifies the inference we made for the kinks in L-I curves in relation to the formation of higher order modes that affects the output characteristics.

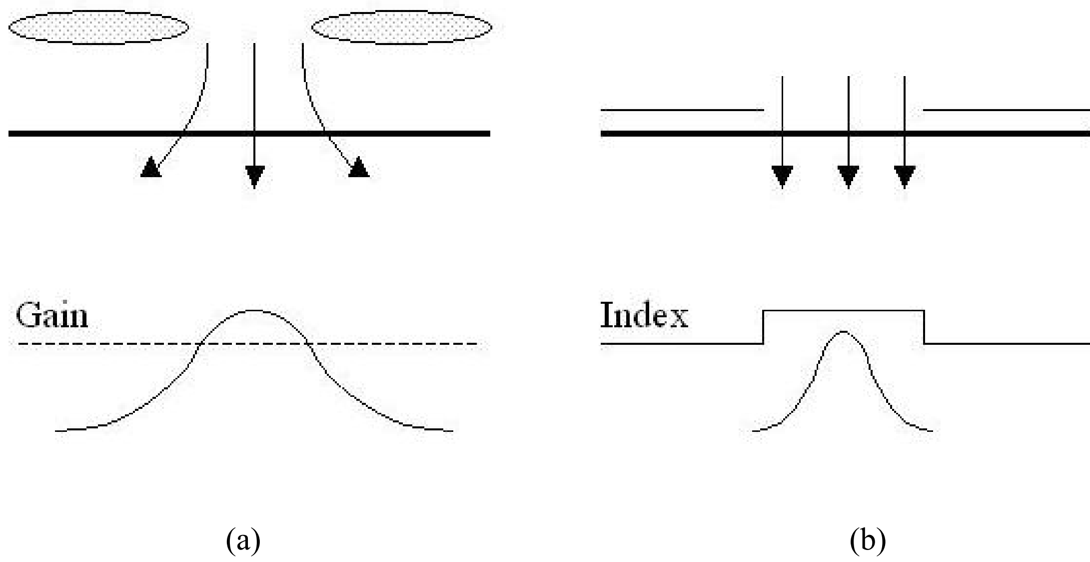

Fig. 4.13 (a) The gain guiding for the implanted VCSEL and (b) the index guiding for the oxidized VCSEL

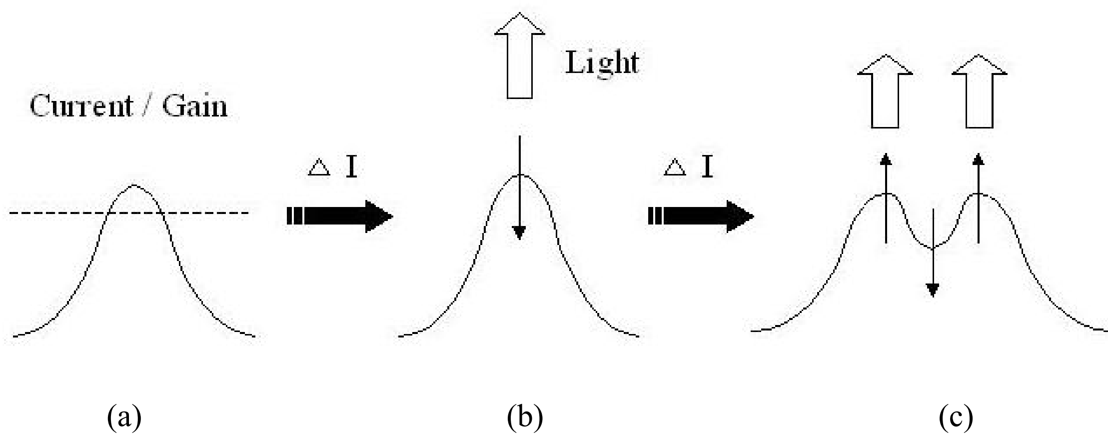

Fig. 4.14 The spatial hole burning effect starts with (a) the initial gain above threshold and (b) the increasing intensity of light reduces the gain in the middle along with the injection current. Finally, (C) the gain in the surroundings eventually above threshold and the higher order mode starts to lase.

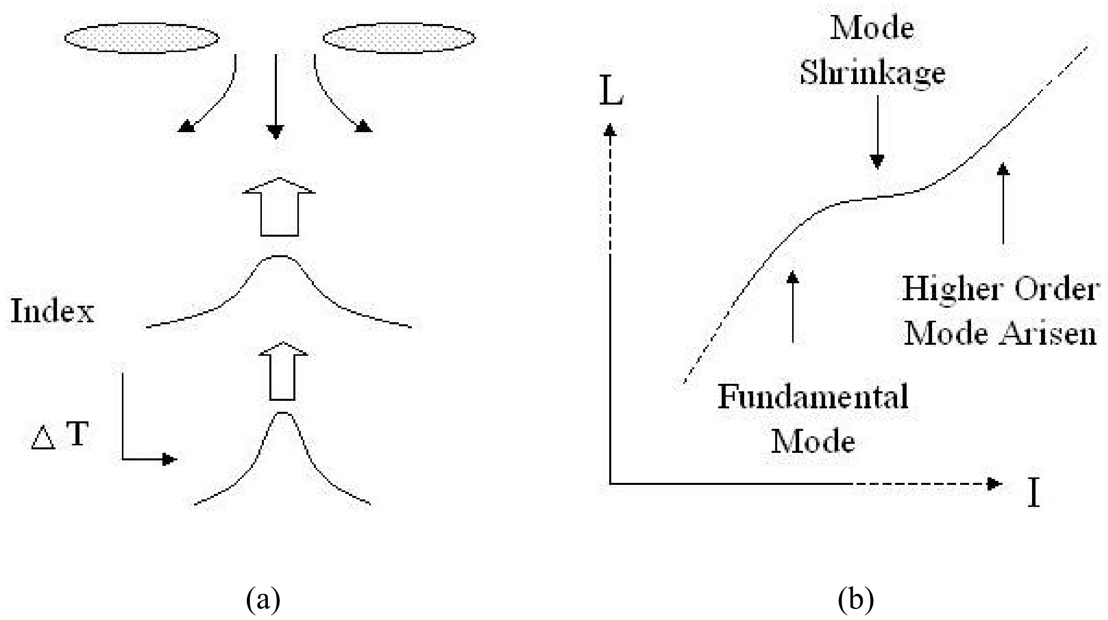

Fig. 4.15 (a) The self-focusing (thermal lens) effect and (b) the kink of the L-I curve corresponding to the transverse mode formation

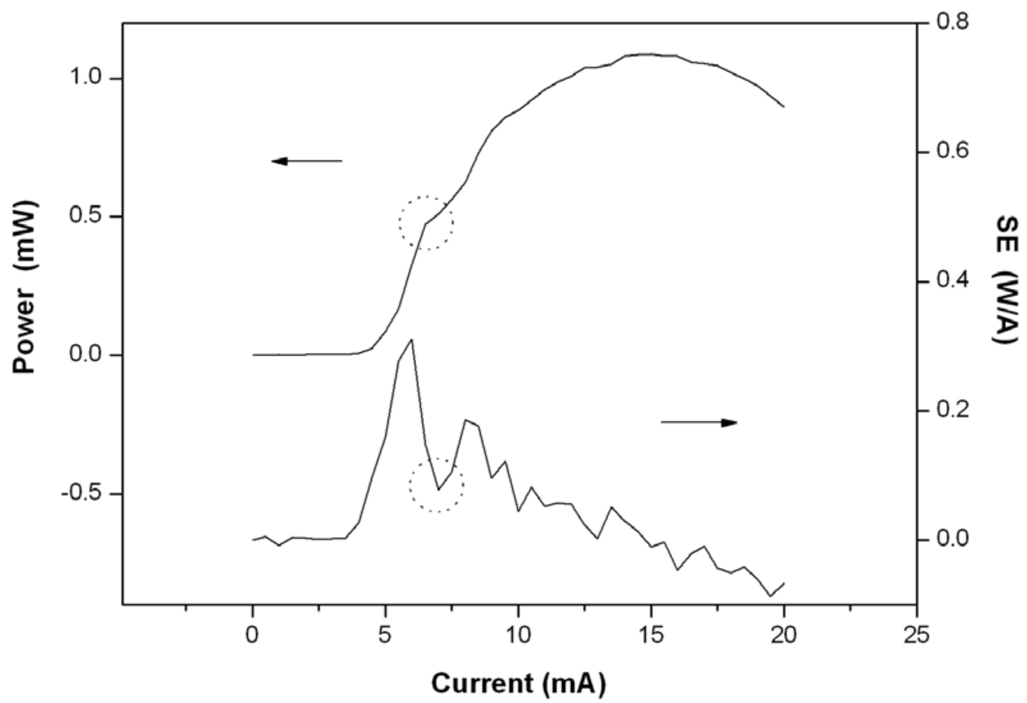

Fig. 4.16 The slope efficiency in relation to the kinks in the L-I curve

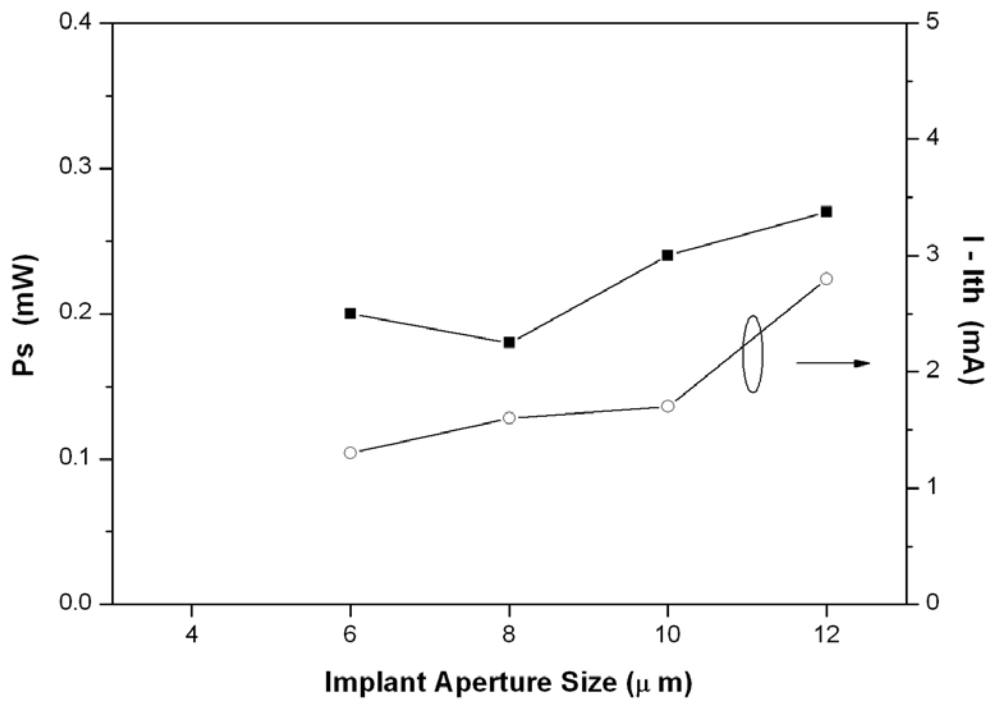

Fig. 4.17 The power, slope efficiency, and the current range according to the selected bias point in the devices with different implant aperture sizes

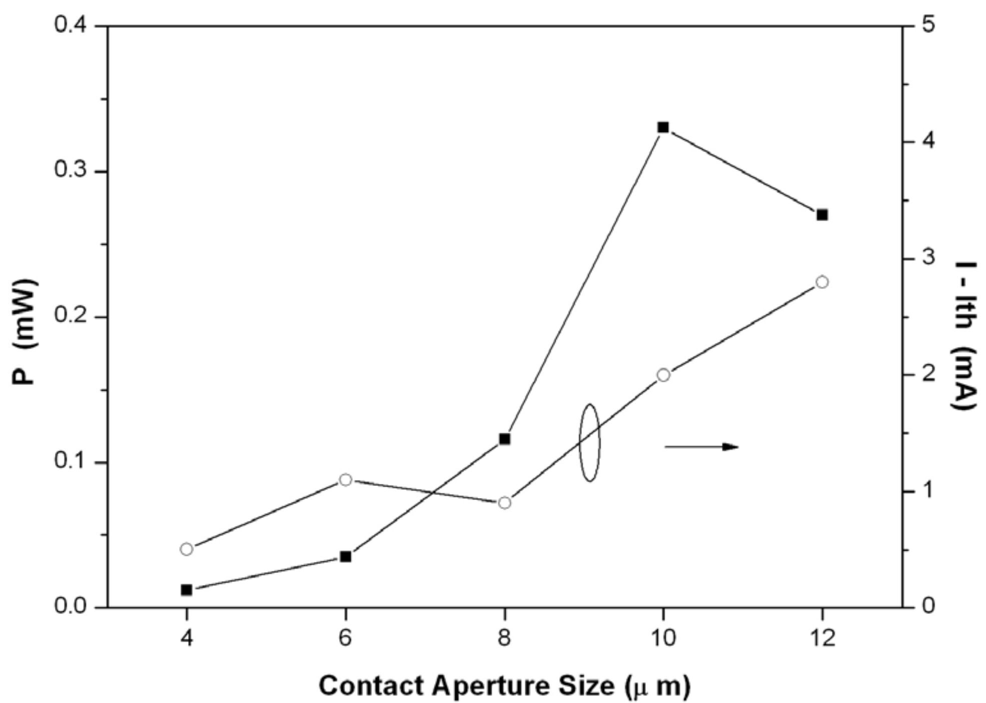

Fig. 4.18 The power, slope efficiency, and the current range according to the selected bias point in the devices with different contact aperture sizes

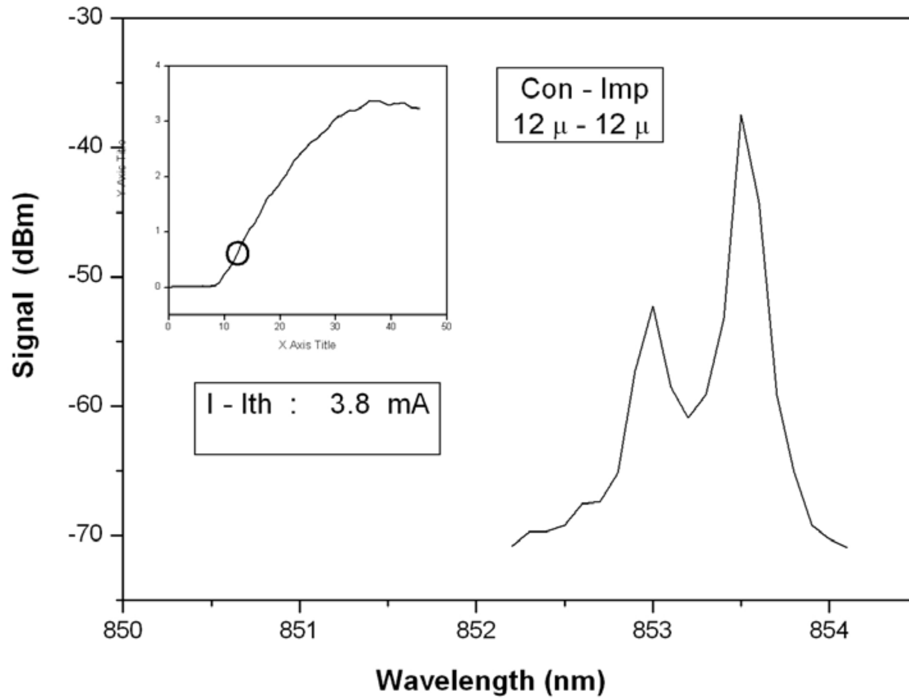

Fig. 4.19 The power, current range, and spectrum according to the selected bias point in the 12-12 um device

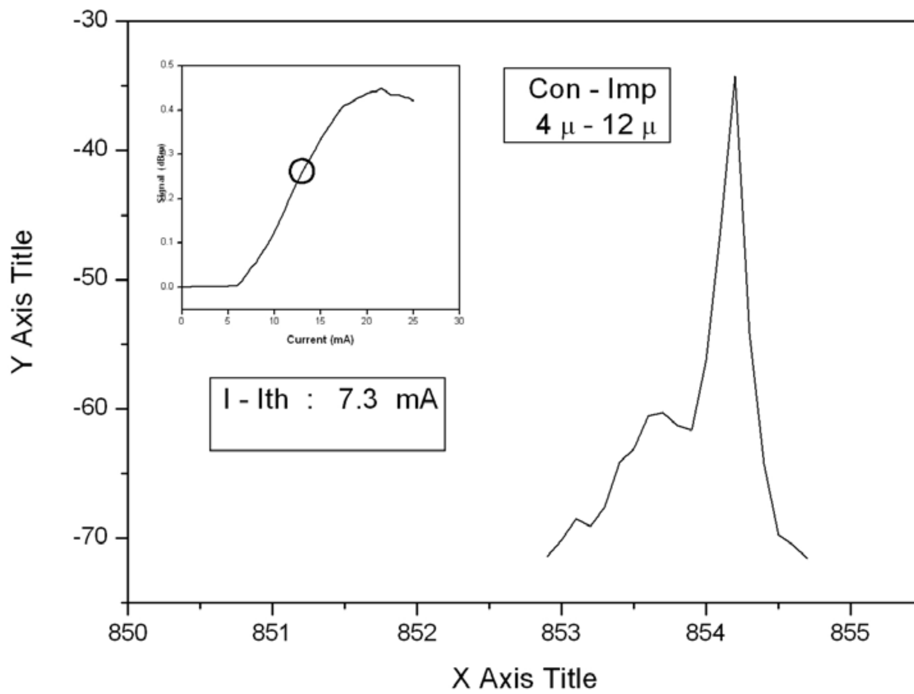

Fig. 4.20 The power, current range, and spectrum according to the selected bias point in the 4-12 um device

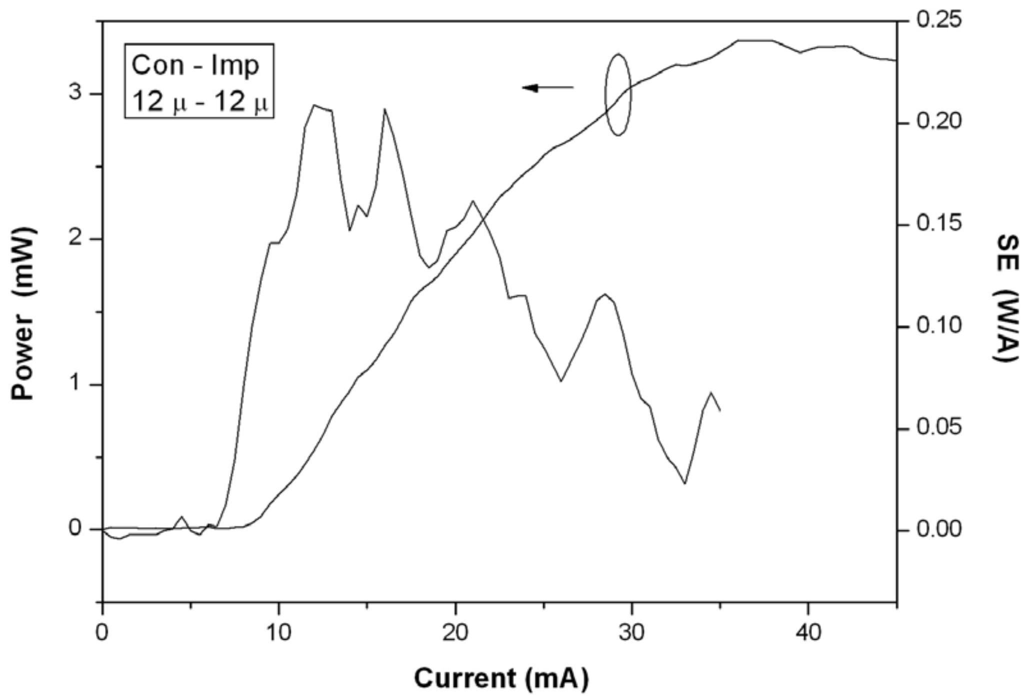

Fig. 4.21 The variation of the slope efficiency in the L-I curve from threshold to roll-over in the 12-12 um device

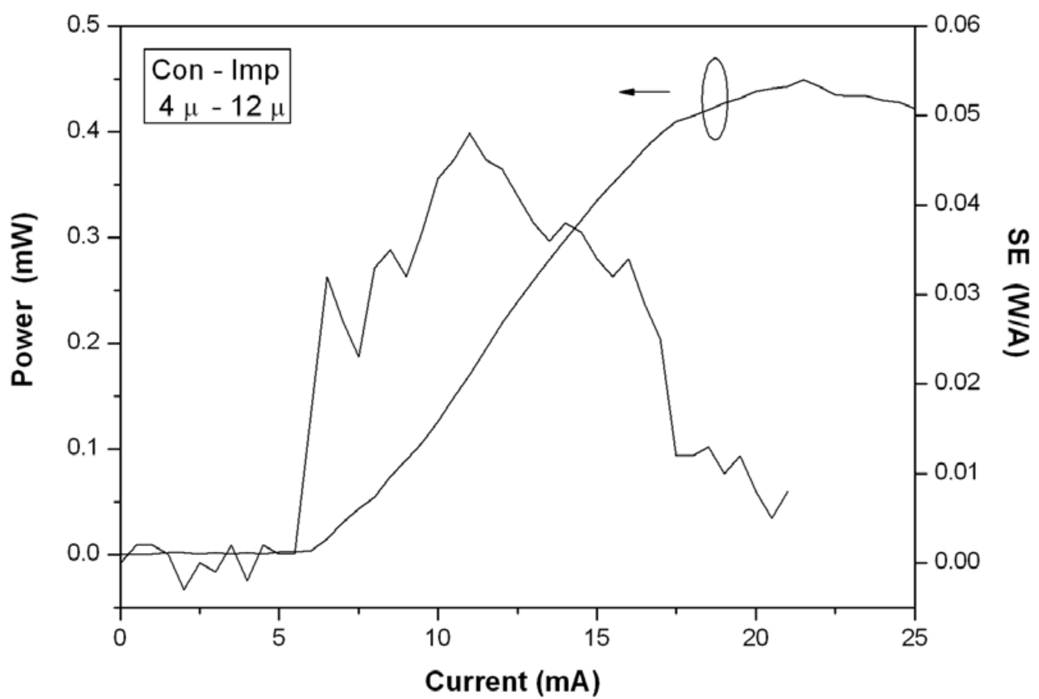

Fig. 4.22 The variation of the slope efficiency in the L-I curve from threshold to roll-over in the 4-12 um device

Chapter 5

Conclusion

We have used a different process method to have SiO_2 deposited before ion implantation and evaporated the metal contact with pad at the same time discriminated from the traditional method with metal contact evaporation before ion implantation. The completed devices worked successfully and the wafer-level testing was performed under continuous-wave operation at room temperature.

The projection range of ion implantation for the devices with different SiO_2 thickness is discussed. The smaller difference in ion implantation depth in the device with thinner SiO_2 is less affected to the current confinement. It can be seen by the fact that from the output characteristic of the device with larger SiO_2 thickness, the higher threshold current implies the existence of current leakage with poor performance in light output power.

The L-I-V characteristics of the devices with different implant and contact apertures are discussed. For the device with smaller implant aperture, the series resistance is larger and the narrower current passage produces higher current density (gain) in a result of lower threshold current, peak power, and current range from threshold to roll over condition with more resistive heating. For the device with smaller contact aperture, the series resistance is about the same to others and the threshold current, peak power, and current range from threshold to roll-over condition are all smaller due to the lateral current spreading and the light suppression by smaller contact opening.

The emission spectrum of the implanted VCSEL is provided and the wavelength characteristics of transverse modes are discussed. The higher order transverse mode tends to be shorter in wavelength and the red shift of all modes at higher injection current due to the thermal dependence on energy gap is observed.

The transverse mode formation in relation to the kinks in L-I curves for implanted VCSELs is discussed. We select a current bias point at the first local minimum of the variant slope efficiency in each L-I curve above threshold to represent the maximum single-mode condition. For the device with smaller implant aperture, the output power and current range referred to this bias point are smaller due to more thermally induced index grading in the active region with self-focusing effect.

Applying the same method to the devices with decreasing contact apertures, the reduction of current range does not conform to the expectation that the higher order mode suppression in the periphery by the contact layer should extent the operating current range for light output with same transverse mode behavior. We observe the characteristic of the emission spectrum according to the suppression ratio between the peak values for each device at a selected bias point and get the new results consistent with the expectation.

The fundamental mode size is estimated and the size relation between the mode and the contact aperture is obviously seen from the reductive output power of light. The possible reason for the kink in this situation is not simply the spatial hole burning or thermal lens effect in the active region but also the suppression of light directly by the contact. Finally, we compare the slope variations of different devices and find out that the device with smaller contact aperture has more linear output characteristic with the slope retaining at a relative higher value for a larger current range from threshold to roll-over condition.

The maximum single-mode condition is hypothetically determined by the kink phenomenon in the L-I curve without a formal verification by spectrally resolved near-field investigations. Nevertheless, the inaccurate results obtained from the variant slope efficiency in the L-I curve and the characteristics of the emission spectrum still satisfy the aperture size dependence on those device characteristics reasonably.

References

[1] H. Soda, K. Iga, C. Kitaha, and Y. Suemata, "GaInAsP/InP surface emitting injection lasers," Jpn. J. Appl. Phys., vol. 18, pp. 2329-2330, 1979.

[2] F. Koyama, S. Kinoshita, and K. Iga, "Room-temperature continuous wave lasing characteristics of GaAs vertical cavity surface-emitting lasers," Appl. Phys. Lett., vol. 55, pp. 221-222, 1989.

[3] K. D. Choquette and H. Q. Hou, "Vertical-cavity surface emitting lasers: moving from research to manufacturing." Proceedings of IEEE, 85, 1730-1739, 1997.

[4] M. H. MacDougal, P. D. Dapkus, V. Pudikov, H. Zhao, and G. M. Yang, "Ultralow threshold current vertical-cavity surface emitting lasers with AlAs-oxide-GaAs distributed Bragg reflectors," IEEE Photon. Technol. Lett., vol. 7, pp. 229-231, 1995.

[5] K. L. Lear, K. D. Choquette, R. P. Schneider, Jr., S. P. Kilcoycn, and K. M. Geib, "Selectively oxidized vertical-cavity surface emitting lasers with 50% power conversion efficiency," Electron. Lett., vol. 31, pp. 208-209, 1995.

[6] R. A. Morgan, L. M. F. Chirovsky, M. W. Focht, G. Guth, M. T. Asom, R. E. Leibenguth, K. C. Robinson, Y. H. Lee, and J. L. Jewell, "Progress in planarized vertical cavity surface emitting laser devices and arrays," SPIE 1562: Devices for Optical Processing. SPIE, Bellingham, WA, pp. 149-159, 1991.

[7] R. A. Morgan, K. Kojima, T. Mullally, G. D. Guth, M. W. Focht, R. E. Leibenguth, and M. T. Asom, "High-power coherently-coupled 8 x 8 vertical cavity surface emitting laser array," Appl. Phys. Lett., vol. 61, pp. 1160-1162, 1992.

[8] H. Kressel and J. K. Bulter, "Semiconductor lasers and heterojunction LEDs," Academic Press, 1977.

[9] L. A. Coldren and S. W. Corzine, "Diode lasers and photonic integrated circuits," Wiley, 1995.

[10] C. W. Wilmsen, H. Temkin, and L. A. Coldren, "Vertical-cavity surface-emitting lasers," Cambridge University Press, 1999.

[11] L. A. Coldren, "Lasers and modulators for OEICs," in Integrated Optoelectronics, Academic Press, 1994.

[12] A . Yariv, "Quantum electronics, 3rd ed," Wiley, 1989.

[13] D. I. Babic and S. W. Corzine, "Analytic expressions for the reflection delay, penetration depth, and absorptance of quarter-wave dielectric mirrors," IEEE J. Quantum Electron., vol. 28, pp. 514-524, 1992.

[14] C. Lei, T. J. Rogers, D. G. Deppe, and B. G. Streetman, "ZnSe/CaF_2 quarter-wave Bragg reflector for the vertical-cavity surface-emitting laser," J. Appl. Phys., vol. 69, pp. 7430-7434, 1991.

[15] M. H. MacDougal, H. Zhao, P. D. Dapkus, M. Ziari, and W. H. Steier, "Wide-bandwidth distributed Bragg reflectors using oxide/GaAs multilayers," Electron. Lett., vol. 30, pp. 1147-1149, 1994.

[16] K. L. Lear and R. P. Schneider, Jr., "Uniparabolic mirror grading for vertical cavity surface-emitting lasers," Appl. Phys. Lett., vol. 68, pp. 605-607, 1996.

[17] K. Kojima, R. A. Morgan, T. Mullaly, G. D. Guth, M. W. Focht, R. E. Leibenguth, and M. T. Asom, "Reduction of p-doped mirror electrical resistance of GaAs/AlGaAs vertical-cavity surface-emitting lasers by delta doping," Electron. Lett., vol. 29, pp. 1771-1772, 1993.

[18] S. W. Corzine, R. S. Geels, J. W. Scott, R. H. Yan, and L. A. Coldren, "Design of Febry-Perot surface-emitting lasers with a periodic gain structure," IEEE J. Quan. Electron., vol. 25, pp. 1513-1524, 1989.

[19] J. Ko, E. R. Hegblom, Y. Akulova, N. M. Margalit, and L. A. Coldren, "AlInGaAs/AlGaAs strained layer 850nm vertical cavity lasers with very low thresholds," Electron. Lett., vol. 33, pp. 1550-1551, 1997.

[20] Y. J. Yang, T. G. Dziura, S. C. Wang, W. Hsin, and S. Wang, "Submilliamp continuous wave room temperature lasing operation of a GaAs mushroom structure surface-emitting laser," Appl. Phys. Lett., vol. 56, pp. 1839-1840, 1990.

[21] K. D. Choquette, M. Hong, R. S. Freund, J. P. Mannaerts, R. C. Wetzel, and R. E. Leibenguth, "Vertical-surface surface-emitting laser diodes fabricated by in situ dry etching and molecular beam epitaxial growth," IEEE Photon. Technol. Lett., vol. 5, pp. 284-287, 1993.

[22] W. Jiang, C. Gaw, P. Kiely, B. Lawrence, M. Lebby, and P. R. Claisse, "Effect of proton implantation on the degradation of GaAs/AlGaAs vertical cavity surface emitting lasers," Electron. Lett., vol. 33, pp. 137-139, 1997.

[23] K. D. Choquette, R. P. Schneider, Jr., K. L. Lear, and K. M. Geib, "Low threshold voltage vertical-cavity lasers fabricated by selective oxidation," Electron. Lett., vol. 30, pp. 2043-2044, 1994.

[24] K. M. Geib, K. D. Choquette, H. Q. Hou, and B. E. Hammons, "Fabrication issues of oxide-confined VCSELs," in Vertical-Cavity Surface-Emitting Lasers, 3003, pp. 69-74, SPIE, 1997.

[25] N. K. Dutta, "Analysis of current spreading, carrier diffusion, and transverse mode guiding in surface emitting lasers," J. Appl. Phys., vol. 68, pp. 1961-1963, 1990.

[26] M. A. Afromowitz, "Refractive index of $Ga_{1-x}Al_xAs$," Solid State Comm. 15, 59, 1974.

[27] A. Sharma, J. M. Yarrison-Rice, H. E. Jackson, and K. D. Choquette, "Near-field spectroscopic characterization of a 10um aperture selectively oxidized vertical cavity surface emitting laser," J. Appl. Phys., vol. 92, no. 11, pp. 6837-6844, 2002.

[28] W. T. Silfvast, "Laser fundamentals," Cambridge University Press, 1999.

[29] A. Yariv, "Optical waves in crystals," Wiley, 1984.

[30] J. Kim, D. E. Pride, J. T. Boyd, and H. E. Jackson, "Spectrally-resolved near-field investigation of proton implanted vertical cavity surface emitting lasers," Appl. Phys. Lett., vol. 72, no. 24, pp. 3112-3114, 1998.

[31] E. W. Young, K. D. Choquette, J. P. Seurin, S. L. Chuang, K. M. Geib, and A. A. Allerman, "Comparison of wavelength splitting for selectively oxidized, ion implanted, and hybrid vertical-cavity surface-emitting lasers," IEEE J. Quan. Electron., vol. 39, no. 5, pp. 634-638, 2003.

[32] K. L. Lear, K. D. Choquette, R. P. Schneider, Jr., and S. P. Kilcoyne, "Modal analysis of a small surface emitting laser with a selectively oxidized waveguide," Appl. Phys. Lett., vol. 60, no. 20, pp. 2616-2618, 1995.

[33] C. J Chang, M. Orenstein, A. V. Lehmen, L. T. Florez, J. P. Harbison, and N. G. Stoffel, "Transverse mode characteristics of vertical cavity surface-emitting lasers," Appl. Phys. Lett., vol. 57, no. 3, pp. 218-220, 1990.

[34] D. Vakhshoori, J. D. Wynn, and G. J. Zydzik, "Top-surface emitting lasers with 1.9V threshold voltage and the effect of spatial hole burning on their transverse mode operation and efficiencies," Appl. Phys. Lett., vol. 62, no. 13, pp. 1448-1450, 1992.

[35] G. C. Wilson, D. M. Kuchta, J. D. Walker, and J. S. Smith, "Spatial hole burning and self-focusing in vertical-cavity surface-emitting laser diodes," Appl. Phys. Lett., vol. 64, no. 5, pp. 542-544, 1993.

[36] N. K. Dutta, L. W. Tu, G.. Hasnain, G. Zydzik, Y. H. Wang, and A. Y. Cho, "Anomalous temporal response of gain guided surface emitting lasers," Electron. Lett., vol. 27, no. 3, pp. 208-209, 1991.

[37] M. Brunner, K. Gulden, R. Hovel, and M. Moser, "Thermal lensing effects in small oxide confined vertical-cavity surface-emitting lasers," Appl. Phys. Lett., vol. 76, no. 1, pp. 7-9, 2000.

[38] R. A. Morgan, G. D. Guth, M. W. Focht, M. T. Asom, K. Kojima, L. E. Rogers, and S. E. Callis, "Transverse mode control of vertical-cavity top-surface-emitting lasers," IEEE Photon. Technol. Lett., vol. 4, no. 4, pp. 374-376, 1993.